Journal of Structural Geology 182 (2024) 105099

Contents lists available at ScienceDirect

Journal of Structural Geology

journal homepage: www.elsevier.com/locate/jsg

Combining traditional and quantitative multiscale structural analysis to reconstruct the tectono-metamorphic evolution of migmatitic basements: the case of the Valpelline Series, Dent-Blanche Tectonic System, Western Alps

F. Caso [a,*], C.B. Piloni [a], M. Filippi [a], A. Pezzotta [a], E. Fazio [b], R. Visalli [b], G. Ortolano [b], M. Roda [a], M. Zucali [a]

[a] Department of Earth Sciences "A. Desio", University of Milan, Via Mangiagalli 34, 20133, Milan, Italy
[b] Department of Biological, Geological and Environmental Sciences, University of Catania, Corso Italia, 57, 95129, Catania, Italy

ARTICLE INFO

Keywords:
3D outcrop models
Quantitative multiscale structural analysis
X-ray maps
High-temperature deformation
Migmatites

ABSTRACT

Due to the ongoing development of new technologies, many instruments are available to assist geological investigations at different scales. These techniques, including 3D outcrop modelling from aerial photogrammetry and quantitative microstructural analysis are useful in crystalline basements studies. This contribution combines traditional and quantitative multiscale structural analysis techniques to the migmatitic rocks of the Valpelline Series (Dent-Blanche Tectonic System, Western Alps). Conventional structural analysis is integrated with the extraction of structural data from 3D models of representative smooth outcrops. Quantitative microstructural and mineral-chemical analyses are combined to link structural and metamorphic evolution. This approach allows identifying and correlating foliations that developed during three tectono-metamorphic stages. The first (D_1) includes solid-state deformation associated with an early foliation (S_1) preserved within metabasite boudins enclosed in migmatite gneiss. The second (D_2) is related to the dominant foliation in migmatite gneiss (S_2), coeval with the regional scale anatexis and growth of garnet and cordierite. The third (D_3) is related to the late folding of S_2 and the development of a sillimanite-rich axial plane foliation (S_3) which wraps around garnet and cordierite. Finally, this work discusses pros and cons of each innovative methodology, still emphasising the importance of using manually acquired field data as ground control.

1. Introduction

In the last two decades, new methods including remote sensing techniques and on-field data acquisition using smartphones and tablets (e.g., Lee et al., 2013; Field-Move app; Midland Valley, 2015), are changing the way geoscientists collect data in the field (e.g., Zerboni et al., 2015; Tavani et al., 2022; Misra and Mukherjee, 2023). In particular, there is a growing accessibility to high-resolution satellite imagery (e.g., Perego et al., 2011), and it is relatively easy to acquire photogrammetric images using different instruments. These range from digital cameras equipped with LiDAR (Laser Imaging Detection and Ranging) sensors to UAVs (Unmanned Aerial Vehicles). The development of relatively small and low-cost UAVs permits the high-resolution mapping of areas and their 3D reconstruction, especially when no LiDAR data can be retrieved (e.g., Forti et al., 2023). One of the most common techniques of digital photogrammetry is the Structure from Motion (SfM), which permits to reconstruct a 3D structure from bidimensional photographs. The 3D models obtained by these techniques encompass valuable data for structural geology (e.g., Tavani et al., 2014, 2016; Cawood et al., 2017; Mattéo et al., 2021), geomorphology (Bonasera et al., 2022, 2023; Misra and Mukherjee, 2023), and archaeometry (Brandolini et al., 2020). All these approaches are particularly effective in Alpine environments undergoing deglaciation, where the absence of vegetation cover and the smoothness of the outcrops permit a clear exposure of rocks and structures.

Many studies used these techniques to extract structural data such as orientations of foliation surfaces, fold axes, and fractures. The results remain reliable even when compared to handheld measured data,

---

* Corresponding author.
E-mail address: fabiola.caso@unimi.it (F. Caso).

https://doi.org/10.1016/j.jsg.2024.105099
Received 28 August 2023; Received in revised form 18 January 2024; Accepted 7 March 2024

typically exhibiting a mismatch of approximately 5° in dip values and 10°–15° in dip azimuth (e.g., Cawood et al., 2017; Novakova and Pavlis, 2017). This approach may be particularly useful in such environments where obtaining a statistically significant number of orientations for structural calculations (e.g., fold analysis, fractures analysis; Ramsay and Huber, 1987; Cawood et al., 2017) may be complex due to several factors. These include (i) the geographical location of the outcrops at high altitudes and/or with snow coverage, making them accessible only for a few months during the year and only a few hours a day; (ii) outcrops located on vertical cliffs that are completely inaccessible for traditional data measurements and sampling. In these situations, aerial photogrammetry with drones and/or 3D outcrop modelling through cameras equipped with LiDAR sensors are very helpful. Indeed, this approach allows also to extend the dimensions of the study area up to the hectometer scale.

In the last years, several innovative methodologies have been also improved for microstructural and mineral-chemical analysis of crystalline basements (e.g., Corti et al., 2019; Visalli et al., 2021; Zucali et al., 2021; Caso, 2023; Fazio et al., 2024) that are facilitating the quantitative digital transition of fabric and petrological rock parameters acquisition. These techniques include the extraction of quantitative grain shape parameters from thin sections by semi-automatic segmentation (Heilbronner, 2011; Heilbronner and Barrett, 2014; Corti et al., 2019; Visalli et al., 2021) and quantitative chemical data extraction from Electron MicroProbe Analyzer (EMPA) X-ray maps and point mineral-chemical analyses (e.g., XMapTools: Lanari et al., 2014; Lanari et al., 2019; Q-XRMA: Ortolano et al., 2018). The combination of these two techniques is effective in discriminating different generations of superimposed structures and defining tectono-metamorphic stages (e.g., Corti et al., 2019; Roda et al., 2021; Zucali et al., 2021; Caso, 2023).

The goal of this work is to combine these analysis techniques developed to operate at different scales. Indeed, a reliable reconstruction of the tectono-metamorphic evolution of crystalline basements requires a multiscale approach to collect and analyse structural data, specifically foliations and folds associated with superimposed deformation stages. In this situation, is also fundamental the identification of the mineral assemblages supporting each structure (e.g., Spalla, 1993; Johnson and Vernon, 1995; Zucali et al., 2002; Passchier and Trouw, 2005; Spalla et al., 2005). Moreover, these techniques aid in the targeted choice of meso- and microstructural domains with different deformation and metamorphic transformation degrees (e.g., coronitic, tectonitic and mylonitic domains; Salvi et al., 2010; Gosso et al., 2015; Zucali et al., 2020), aimed at reconstructing the whole tectono-metamorphic history.

The use of modern quantitative techniques may be particularly useful in the study of migmatitic basement rocks, characterised by complex structural patterns derived from the interplay between metamorphic, magmatic, and deformative processes under transient conditions (Brown, 1973; Hopgood, 1979; Ashworth, 1985; Kriegsman, 2001; Sawyer, 2001, 2008; Kreigsman and Alvarez-Valero, 2010; Yakymchuk, 2020). In fact, multiple partial melting events and the complex geometrical patterns resulting from melt migration (Sawyer, 2001) complicate the reconstruction of the tectono-metamorphic evolution of these basements. Consequently, it is often difficult to reconstruct the relative chronology of the deformation events during high-temperature (H*T*) evolution through traditional "field-based only" structural analysis. However, a multidisciplinary and multiscale approach that combines meso- and microscale analysis supported by mineral-chemical data using different new approaches is still missing.

Therefore, in this study, we choose the migmatitic basement of the Valpelline Series (Dent-Blanche Nappe, Western Italian Alps) as a case study, to envisage a comprehensive view of its structural and tectonothermal evolution. This series represents a fragment of the pre-Alpine lower continental crust that underwent H*T* deformation and partial melting during Permian lithospheric extension (Zucali et al., 2011; Pesenti et al., 2012; Manzotti and Zucali, 2013; Caso, 2023; Roda et al., 2023; Caso et al., 2024).

2. Geological setting

The Alps (Fig. 1a) are one of the peri-Mediterranean mountain ranges originated from the subduction of the Ligurian-Piedmont Ocean during the Cretaceous and collision between the Adria and European plates in the Eocene (Dewey et al., 1989; Schmid et al., 2004; Beltrando et al., 2010; Handy et al., 2010; Lardeaux, 2014; Angrand and Mouthereau, 2021). The Austroalpine and Penninc domains constitute the axial zone of the Alps, whose oceanic and continental rocks underwent high-pressure and low-temperature metamorphism during the Alpine subduction.

The Dent-Blanche Tectonic System (DBTS; Manzotti et al., 2014a; Manzotti and Ballèvre, 2017) belongs to the Austroalpine domain and overlies the oceanic units. The DBTS is traditionally divided into the Dent-Blanche s.s. to the northwest and the Mont-Mary Nappe to the southwest separated by a km-scale mylonitic zone, the Roisan-Cignana Shear Zone (RCSZ, Fig. 1b; Zucali et al., 2011; Manzotti et al., 2014a, b). The Dent-Blanche s.s consists of a Paleozoic basement corresponding to the Arolla and the Valpelline series (Diehl et al., 1952; Manzotti and Zucali, 2013; Manzotti et al., 2014a) which recorded both pre-alpine and alpine metamorphism. The Arolla Series is made of Permian metagranitoid, metagabbro and pre-Permian lenses of migmatite gneiss. Alpine metamorphism and deformation are more pervasive in the Arolla Series than in the Valpelline Series. In particular, in the Arolla Series the Alpine metamorphism developed under blueschists-facies conditions (Roda and Zucali 2008, 2011; Manzotti et al., 2014a, 2014b, 2020). Conversely, the Valpelline Series (VP) better preserves Permian structures and metamorphic assemblages (Zucali et al., 2011; Pesenti et al., 2012; Kunz et al., 2018) from the amphibolite-to granulite-facies conditions (Gardien et al., 1994; Manzotti and Zucali, 2013; Caso, 2023; Caso et al., 2024).

The VP consists of migmatitic metapelites, including Grt–Crd- (abbreviations hereafter are according to Whitney and Evans, 2010) and Grt–Opx-migmatite gneiss, and sillimanite-gneiss, plus felsic granulite. Metasedimentary and felsic rocks are associated with Grt–Cpx-amphibolite also locally affected by partial melting (black amphibolite in Fig. 2a), minor pegmatites and aplites, basic granulites and marbles (Diehl et al., 1952; Nicot, 1977; Gardien et al., 1994; Manzotti and Zucali, 2013; Caso et al., 2024). In the VP a former tectono-metamorphic stage (pre-D_2 in Manzotti and Zucali, 2013) is marked by a relict foliation preserved in meter-scale metabasite bodies. This stage has developed at $T = 700 \pm 50$ °C and $P = 0.57 \pm 0.11$ GPa (Manzotti and Zucali, 2013). Conversely, Gardien et al. (1994) estimated higher pressure conditions within the kyanite stability field (T = 700–800 °C and P = 0.9–1.0 GPa) for the pre-D_2 stage preserved within garnet cores. D_2 stage is related to the development of the regional foliation S_2 and widespread melting, at $T = 810 \pm 40$ °C and $P = 0.7 \pm 0.01$ GPa (Gardien et al., 1994; Manzotti and Zucali, 2013). S_2 is parallel to the lithological boundaries and strikes NE–SW dipping at high angles. During a later stage ($T = 800 \pm 30$ °C and $P = 0.6 \pm 0.07$ GPa; D_3 in Manzotti and Zucali, 2013), the S_2 is folded, leading to the local development of an S_3 axial plane foliation, marked by the blastesis of biotite and sillimanite both at the meso- and microscale. Gardien et al. (1994) recognised a further migmatitic stage related to the cordierite growth, estimated at T = 650–700 °C and P = ~0.35–0.45 GPa. However, recent microstructural analyses found the presence of cordierite within melt-rich portions developed during D_2 and wrapped by S_3 sillimanite-rich foliation (Caso et al., 2024).

The Alpine deformation in the VP is localized in decameter-to hectometer-wide shear zones (crossed patterns in Fig. 2a) marked by cataclasites and mylonites (Pennacchioni and Guermani, 1993; Roda and Zucali, 2008; Manzotti and Zucali, 2013). The mylonitic foliation is marked by chlorite and white mica and developed under greenschists-facies conditions ($T = 430 \pm 30$ °C and P = 0.3–0.5 GPa; Gardien et al., 1994; Manzotti and Zucali, 2013). Mylonitic rocks occurring at contact with the Arolla Series may be contemporaneous to

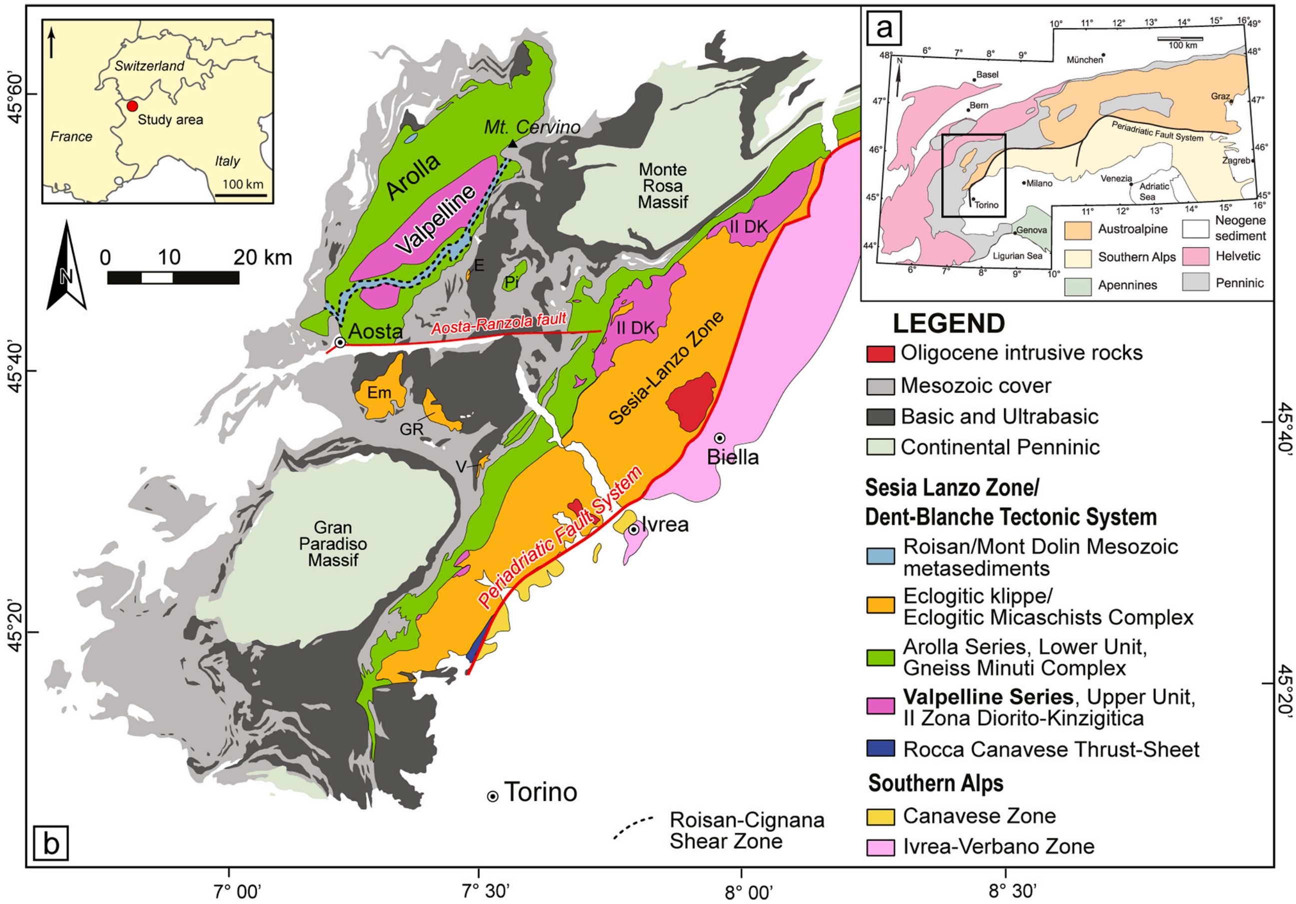

Fig. 1. (a) Tectonic sketch map of the Alps showing the main units; (b) geological map of the Western Alps (modified after Roda et al., 2021). E: Etirol-Lèvaz; Em: Emilius; GR: Glacier Refray; Pi: Pillonet; V: Vanoise; IIDK: II Zona Diorito-Kinzigitica.

the RCSZ shearing, under blueschists-facies conditions (D_3-D_4 stages in Manzotti et al., 2014b). Late stages of Alpine deformation (see D_5 stage in Manzotti et al., 2014b) may be also responsible for the change in orientations of pre-Alpine S_2 and S_3 foliations in the VP, approaching Arolla Series and RCSZ (Dal Piaz et al., 2016; Manzotti et al., 2014b). The precise age of the Alpine metamorphism in the VP is not well-constrained. The whole-rock Rb/Sr ages of Alpine mylonites at the contact between the Arolla and Valpelline series are of ~57 Ma (Angiboust et al., 2014).

3. Methods

3.1. Mesoscale structural analysis

Mesoscale structural analysis has been conducted by combining traditional field observations and measurements with the extraction of data, from UAVs flights and LiDAR point clouds, of the main fabric elements (foliations and dykes orientations). In particular, the orientations of foliations, aplites and pegmatites have been firstly acquired with the compass on the field, together with rock sampling of representative migmatite gneiss for a better constrain of the remote data acquisition. This approach was used in clear and smoother outcrops which represent ideal case studies for 3D outcrop modelling.

SfM technique permitted to develop a 3D model of the selected areas in the VP from 2D images georeferenced in WGS84 coordinates system retrieved with UAV (Westoby et al., 2012; Niedzielski, 2018). The area covered by UAV flight is approximately 40,000 m^2, located at the Lac Mort (see the yellow square in Fig. 2a; coordinates: x: 382,627; y: 5,086, 138; z: 2850 m a.s.l.), on the right slope of the Place Moulin creek Valley. Flights at 15 and 30 m height were made using a Parrot® Anafi drone equipped with a 4k/21 MP camera (Fig. 3a), for the acquisition of ~380 photos, with a resolution of 5344 × 4016 pixels. After that, the photos have been uploaded in Agisoft Metashape version 1.5.5 software (Agisoft Metashape, 2024), and automatically aligned and processed to obtain a point cloud and a mesh model.

Selected outcrops of this area have been scanned through an iPad 11″ Pro equipped with a LiDAR sensor, using the 3D scanner App© (2024), which directly produces a 3D model from a point cloud (Fig. 3b). Both the point clouds derived from the SfM and LiDAR scanning have been exported, reprojected in coordinate metric system (WGS84 – UTM32N) and processed within the CloudCompare software version 2.13 (CloudCompare, 2024), to extract the orientation of the main structural elements. The CloudCompare *Compass* plug-in (Thiele et al., 2017) permits tracing the upper and lower boundaries of a structural element (e.g., including dykes and layers) and produces an interpolated plane that has its dip direction and dip angle (Fig. 3c). Then, the so-obtained structural data were extracted from the software and projected on equal areal stereo plots, together with compass measures, to increase the total number of available structural data and using manual measures as ground control.

The traces of dykes visible from the Google Satellite© imagery were traced and grouped in a vector polyline layer (Fig. 3d), and processed through the *QgSurf* plug-in (https://gitlab.com/mauroalberti/qgSurf) in QGIS version 3.22 (QGIS Development Team, 2024). This tool, using the DEM (Digital Elevation Model) as a base, allowed us to obtain the dip direction and dip angle of a plane which represent the best fit of each traced line intersecting the topographic surface. Then, the data were plotted in an equal areal stereo plot as strikes of the lines calculated from

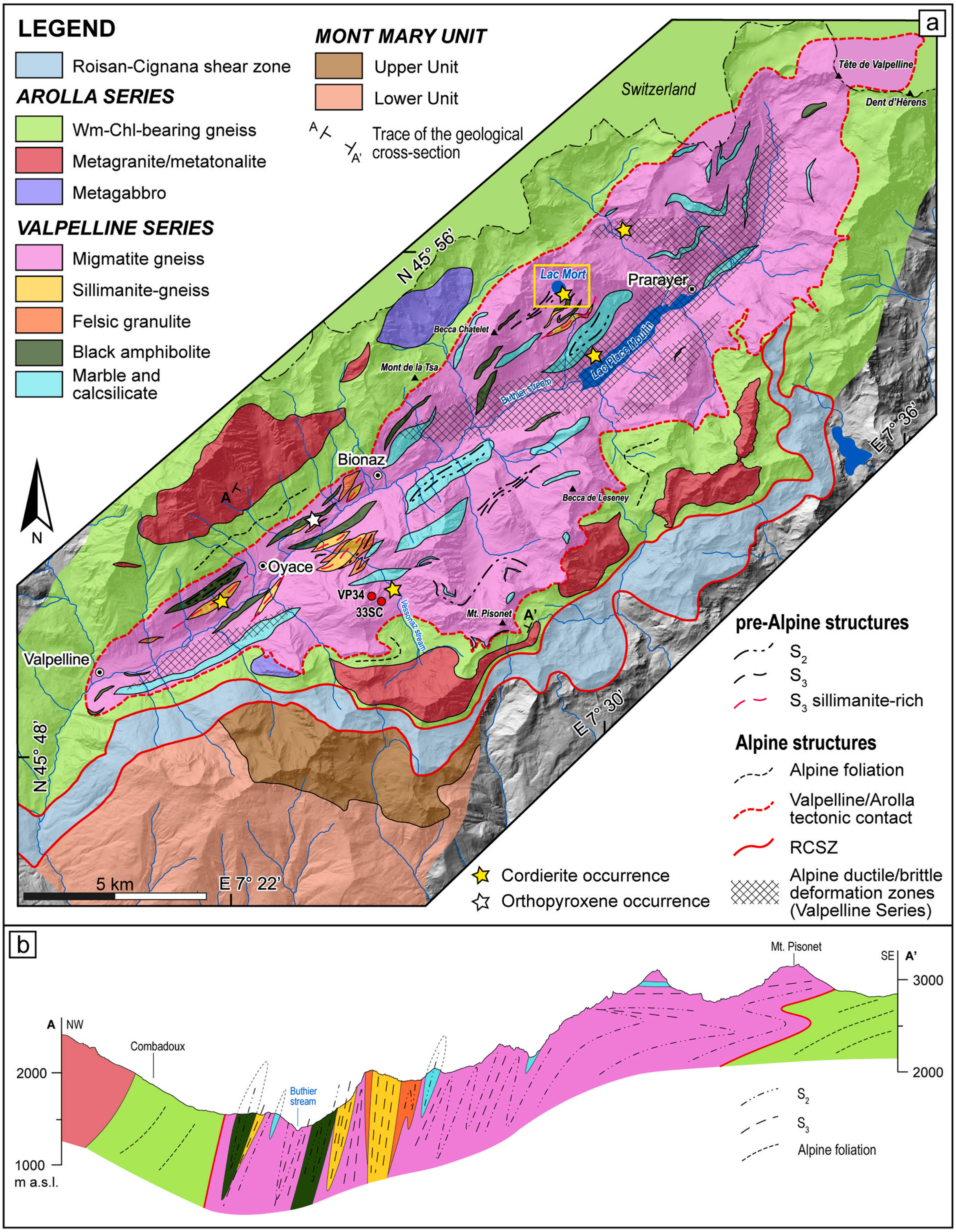

Fig. 2. (a) Geological map of the DBTS (modified from Caso et al., 2024); (b) geological cross-section (A – A′) across the Arolla and Valpelline series.

the dip directions.

3.2. Microscale structural analysis

Two samples for quantitative microstructural analysis have been chosen after analysing at the optical microscope dozens of different migmatite gneiss from different localities of the VP. The chosen samples show different modal proportions, mineral phase distributions and structures. In particular, one sample is representative of a melanosome, and one is representative of a leucosome (33SC and VP34 respectively; see samples location in Fig. 2a), both corresponding to cordierite-migmatite gneiss. First, they were analysed with the optical

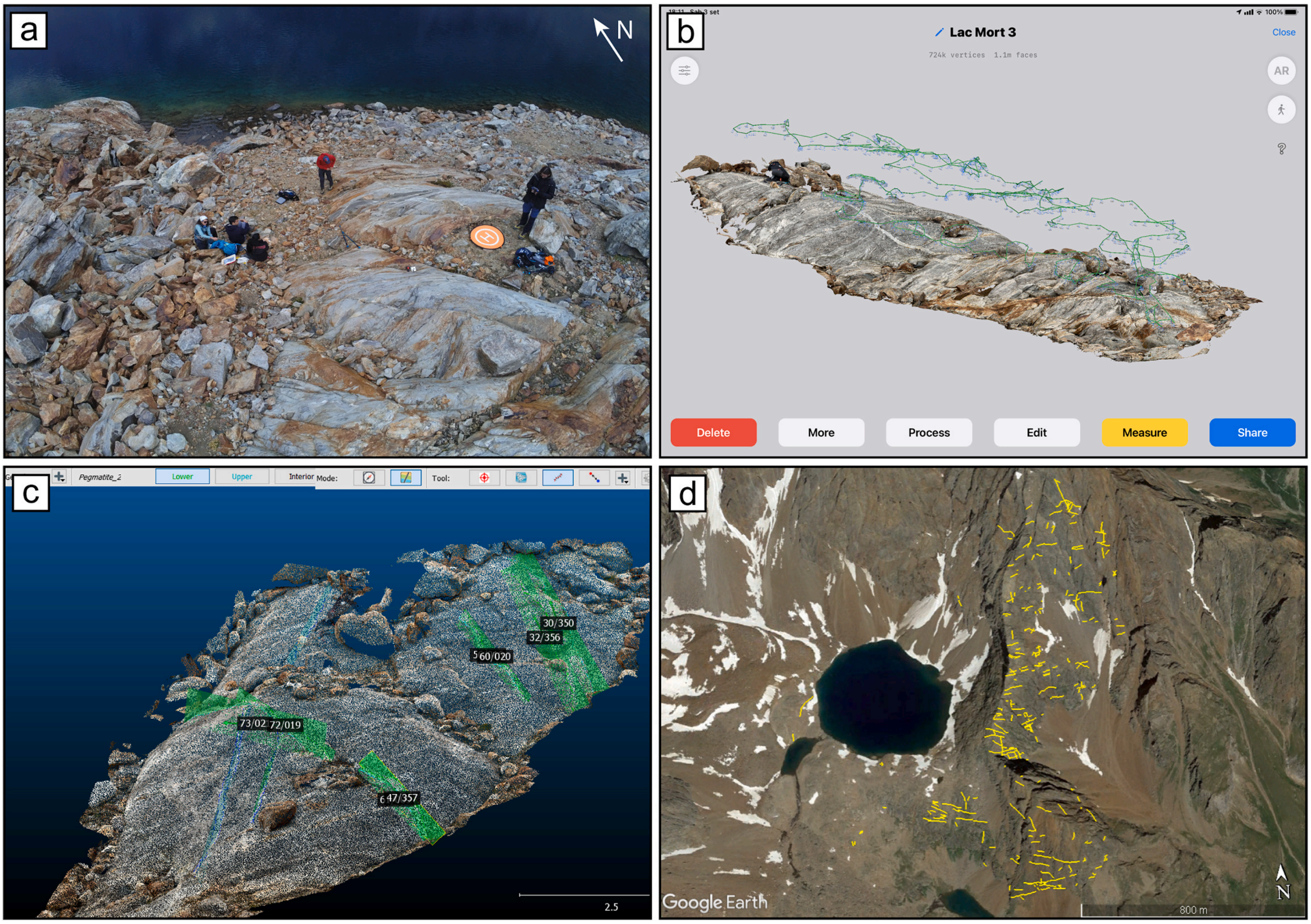

Fig. 3. (a) View of the Lac Mort area during the drone flight; (b) 3D outcrop model acquired through iPad 11″ Pro equipped with LiDAR sensor; (c) point cloud of a 3D outcrop model processed in CloudCompare for the structural data extraction; (d) yellow lines traced on the Google Satellite© in Google Earth to be imported in QGIS for planes extraction. (For interpretation of the references to colour in this figure legend, the reader is referred to the Web version of this article.)

microscope for the reconstruction of the microstructural relations between the different mineral phases, and to define the mineral assemblages marking each recognised fabric element (Passchier and Trouw, 2005; Spalla et al., 2005). The quantitative microstructural analysis was carried out through the Micro-Fabric Analyzer ArcGis toolbox (MFA; Visalli et al., 2021, Fig. 4), used to obtain the vectorial contouring of the mineral grains and measure their shape parameters (see the Appendix A within Visalli et al., 2021 for the explanation of the calculated values).

In detail, the MFA toolbox comprises and uses: (i) the Grain Size Detector (GSD; Fig. 4) which traces vectorial polygonal grains contouring maps by processing and segmenting a high-resolution optical thin section scan (Fig. 4; Visalli et al., 2021); (ii) the Quantitative X-Ray Maps Analyzer tool (Q-XRMA; Ortolano et al., 2018) which derives a mineral classification map obtained from X-ray maps processing (first cycle); (iii) the Mineral-Grain Size Detector (Min-GSD; Visalli et al., 2021) which allows merging the outputs of the GSD and Q-XRMA to label each grain polygon feature with its mineral phase name, since the GSD tool does not separate the grains into different minerals. To apply the latter tool is necessary to geo-reference in ArcGIS the Q-XRMA output on the GSD one. Both the MFA and Q-XRMA toolboxes have been developed at the Geoinformatics and Image Analysis Lab of the Biological, Geological, and Environmental Sciences Department at the University of Catania (Italy).

The thin section scans used in the GSD toolbox were acquired under crossed polarized light by using an Epson V750 dual-lens system scanner at 24 bit-depth and 4800 dpi of resolution corresponding to a pixel size of ~5.29 μm. These settings for this device represent the best compromise between high-quality imaging, relatively fast image-processing time, and reasonable hard drive space storage (Visalli et al., 2021).

Among the obtained shape parameters, the long axis orientation (values between 0°–180°) and the roundness (see Supplementary Material 1 for all the obtained shape parameters) have been used for the distinction of different microstructures marked by different mineral generations. In particular, the long axis orientation is the angle between a vertical reference (in this case roughly perpendicular to the main foliation of the thin section, depending on the thin section scan orientation) and the long axis of each mineral grain, measured clockwise. Therefore, in this case, grains marking the main foliation will have orientations of ~90°.

3.2.1. *Mineral-chemical analysis*

Quantitative mineral-chemical points analysis and X-ray chemical maps of major (Si, Ti, Al, Fe, Mn, Mg, Ca, Na, K) and minor elements (Cr) have been acquired using the Electron Microprobe Analyzer (EMPA) JEOL 8200 Superprobe WDS at the Dipartimento di Scienze della Terra "A. Desio" – Università degli Studi di Milano. For sample 33SC the Fe, Mg, Ti, Ca and Na maps were acquired using five wavelength-dispersive spectometers (WDS) detectors, while Si, Al, Mn, Cr and K maps using an energy-dispersive spectrometer (EDS) detector. These maps were acquired using a beam current of 100 nA, with a dwell time of 55 ms and a resolution 1024 × 600 pixels (35 μm of step size). For sample VP34 four element maps were acquired (Al, Fe, K, Na) using four WDS detectors.

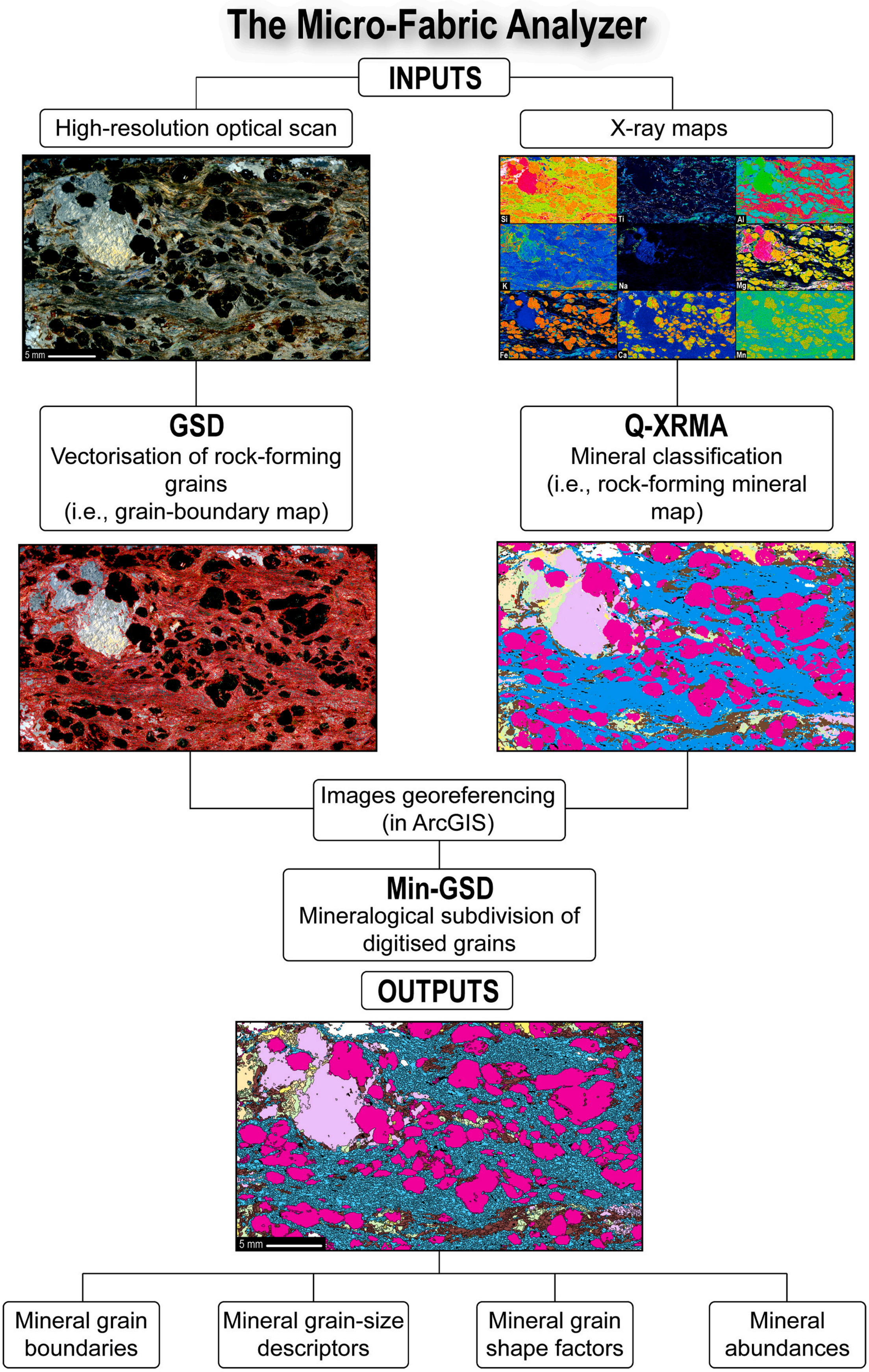

Fig. 4. Micro-Fabric Analyzer workflow (modified after Visalli et al., 2021; Caso, 2023).

These maps were acquired using a beam current of 50 nA, a dwell time of 15 ms and a resolution of 1024 × 512 pixels (pixel size of 35 μm). For quantitative mineral-chemical points analyses, an accelerating voltage of 15 KeV and 50 nA of beam current was used. These were used as internal standards in the Q-XRMA tool (second cycle; Ortolano et al., 2018; Corti et al., 2019; Roda et al., 2021; Zucali et al., 2021; Caso, 2023) to obtain calibrated mineral maps showing the element content (expressed in atoms per formula unit; apfu) for selected mineral phases (biotite and garnet). By doing so, it was possible to highlight chemical variations and zoning of crystals within different microstructural sites and use them to better constrain the tectono-metamorphic evolution of the study area.

The tectono-metamorphic stages are named using a numerical progression (e.g., D_1, D_2, etc.). The prefix D-stands for deformation, S- indicates foliation, A- fold axis, F- fold, and A.P.- stands for axial plane. Mineral formulae were calculated according to Deer et al. (1992) and using pyMinColab v.2023 (Zucali, 2023).

4. Rock types

The Valpelline Series is mostly made by metapelites, including migmatite gneiss and sillimanite-gneiss. Migmatite gneiss is the most common rock type and comprises both stromatic diatexites and metatexites. Most migmatites are garnet-bearing, but in different localities of the valley cordierite–garnet-bearing migmatite gneiss also occurs (see yellow stars in Fig. 2a; Gardien et al., 1994; Manzotti and Zucali, 2013; Caso, 2023; Caso et al., 2024). More rarely, garnet–orthopyroxene-bearing migmatite gneiss are also found (see red star in Fig. 2a; Caso et al., 2024). Sillimanite-gneiss and minor felsic granulites occur as decametric to hectometric bodies interlayered with migmatite gneiss. Metabasic rocks correspond to basic granulites and brown amphibolites occurring in meter-sized lenses/boudins embedded in migmatite gneiss, and black amphibolite occurring as hectometric bodies interlayered with metapelites, and locally affected by partial melting. Marble and calcsilicatic rocks also crop out as hectometric bodies interlayered with metapelitic rocks and black amphibolites (Fig. 2a; see Caso et al., 2024 for detailed lithological description).

In particular, in the Lac Mort area covered by LiDAR and UAVs flights (Fig. 2a), two main groups of lithologies occur: (i) basic granulite and brown amphibolite and (ii) cordierite-bearing migmatite gneiss. In particular, the rocks of the former group crop out as meter-sized levels or boudins embedded in the cordierite-migmatite gneiss (not mappable at the map resolution scale; Fig. 2a) and locally folded.

Basic granulite shows a granoblastic to slightly gneissic fabric made by the isorientation of orthopyroxene and clinopyroxene and minor whitish plagioclase-rich aggregates. Brown amphibolite has a more pronounced gneissic structure made by the isorientation of brown amphibole and millimetric plagioclase. Cordierite-migmatite gneisses here mainly correspond to metatexites, showing a gneissic texture made by alternating leucosomes and melanosomes, which follows the regional foliation trend and lithological boundaries. The paleosome locally occurs as fine-grained pluridecimetric levels made of pyroxene, amphibole, biotite and plagioclase, similar to basic granulites. Melanosomes include millimetric isoriented biotite and minor millimetric fibrous sillimanite defining the main foliation. Leucosomes are made of fine-grained plagioclase, quartz and locally minor K-feldspar. They show variable thickness, from centimetric to pluricentimetric, occurring as regular levels parallel to the main foliation, locally folded, or plurimetric pods with irregular shapes. Locally, a second generation of leucosome makes irregular patterns cross-cutting the main fabric (the main melanosome-leucosome alternation parallel to the regional foliation). Garnet occurs as millimetric to pluri-millimetric reddish porphyroblasts both in the melanosomes and leucosomes, together with cordierite. The latter constitutes dark-grey porphyroblasts from pluri-millimetric to centimetric. Within migmatites pluri-centimetric to metric lenses and boudins of fine-grained migmatitic gneiss also occur. They have a granoblastic structure made of plagioclase, quartz and minor garnet. Also, these portions, together with the migmatitic gneiss are cross-cut by centimeter-thick and discordant leucosomes.

As stated above, cordierite-migmatite gneisses were detected in several localities of the VP (see yellow stars in Fig. 2a). Nevertheless, it is hard to find fresh cordierite crystals suitable for reliable microstructural investigation and mineral analysis at the EMPA. Indeed, most of the recognised cordierite blasts in thin sections are characterised by local or complete transformation into fine-grained white mica or chlorite aggregates (Fig. 5) during late retrogression (pinitisation; Seifert and Schreyer, 1970; Ogiermann and Kalt, 2000). The two selected samples analysed in this work have been chosen from the Comba Vessonaz area (red dots in Fig. 2a) since they show freshly preserved cordierite. Sample VP34 is representative of a melt-rich portion, while the 33SC shows a well-developed sillimanite-rich foliation suitable for microstructural constraints. Samples collected at the Lac Mort area (where the mesostructural study has been carried out) showed strongly retrogressed cordierite and were not homogeneous or suitable for the tectono-metamorphic reconstruction.

5. Results

5.1. Traditional mesostructural analysis

Together with field observations, (Fig. 6) a number of 154 orientations of structural elements has been derived from compass measurements (Fig. 7).

The S_1 foliation is the internal foliation of basic granulite and brown amphibolite boudins wrapped by the S_2, locally geometrically discordant to the long axis of the boudin and S_2 (Fig. 6a). In particular, at the mesoscale, S_1 has been detected in correspondence F_2 isoclinal folds, where this foliation is not completely transposed (Fig. 6b). In the basic granulite boudins, S_1 is a layering marked by the isorientation of pyroxene- and plagioclase-rich domains and by amphibole-rich and plagioclase-rich domains in the brown amphibolites. S_1 dips mainly toward SE, with variable but relatively high dip angles (Fig. 7a). The mean orientation from field data, calculated from the Kamb contouring is 164/55°.

S_2 foliation is penetrative in migmatite gneiss. It is defined by the alternation between melanosomes and leucosomes, and by the isorientation of biotite and sillimanite. S_2 dips mainly toward the S–SE with variable dip angles, which are locally sub-vertical. Locally it also dips toward the NW sub-vertically (Fig. 7c). The mean orientation calculated from the Kamb contouring field data is 142/54° (dip direction and dip angles). A_2 axes, folding S_1, trend toward S–SW and plunge at 60–80°; A.P.$_2$ axial planes dip toward S–SE with almost sub-vertical dip angles (Fig. 7e). S_2 is widely deformed and folded by isoclinal (Fig. 6c and d) to open (Fig. 6e) F_3 folds, locally asymmetric, with a W-vergence (Fig. 6e). In correspondence with the isoclinal folds, S_2 and leucosomes are folded, and S_3 axial plane foliation locally develops (Fig. 6d). S_3 dips toward SE, with relatively high dip angles (Fig. 7g). Cordierite is also deformed in correspondence of fold hinges, here occurring as dark-grey aggregates (Fig. 6c). Locally, centimetric-thick leucosomes cross-cut S_2 foliation, along the limbs of F_3 folds (Fig. 6e). These leucosomes also cross-cut the basic granulite boudins, making “a-type” flanking structures with a top-to-the W sense of shear, with the leucosomes behaving as a cross-cutting element (CE; Hudleston, 1989; Mukherjee, 2014, Fig. 6f). The centimeter-thick leucosomes discordant to the S_2 dip toward E–SE and locally toward WSW (Fig. 7f). In some outcrops the F_3 folding produces a crenulation cleavage S_3 (Fig. 6g). A_3 fold axes trend toward the S and plunge at 50–88°; A.P.$_3$ axial planes dip toward the SE with dip angles ranging between ~45 and 75° (Fig. 7g). Kfs-Qz pegmatites and aplites, with different orientations and crosscutting relationship with the above-described structures, occur. The mineralogy between the different systems is the same. One system of dykes is parallel to the migmatitic foliation S_2 and is locally affected by boudinage (Fig. 6h);

Sample	*Crd-locality*	*WGS coordinates*	*main features*	
22CBP10	Grand Place, d'Orein stream	7.5035526 45.9372687	Foliation defined by Bt. Crd is strongly pinitised.	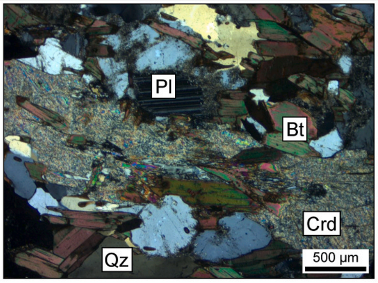
6CP 29SC 31SC 38SC	N of Lac Mort S of Lac Mort S of Lac Mort S of Lac Mort	7.4827177 45.9213619 7.4860345 45.9189366 7.48707993 45.91875192 7.48600577 45.91895677	Foliation defined by Bt and locally minor fibrous Sil. Crd is strongly pinitised	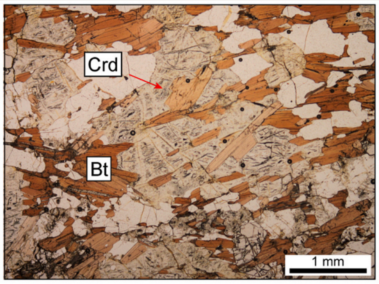
I_22_07 I_28_07	Lac Place Moulin Lac Place Moulin	7.4991744 45.9032835 7.506861 45.907447	Foliation defined by Bt and minor Sil. Crd is strongly pinitised	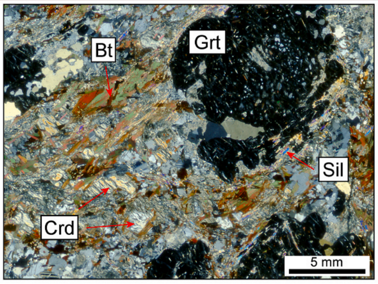
22FC17A	Localitè La Ruine	7.364324 45.839654	Foliation defined by Bt and minor Sil. Crd is strongly pinitised	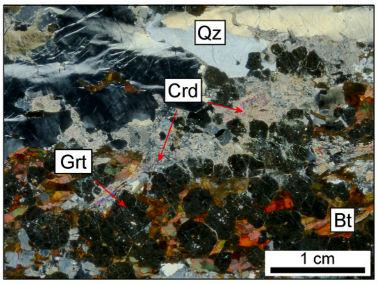
VP34 VP44 33SC	Comba Vessonaz Comba Vessonaz Comba Vessonaz	7.4238788 45.8425377 7.4236035 45.8424476 7.4268945 45.8418167	Foliation defined by Sil and Bt. Crd idiomoprhic and always well preserved.	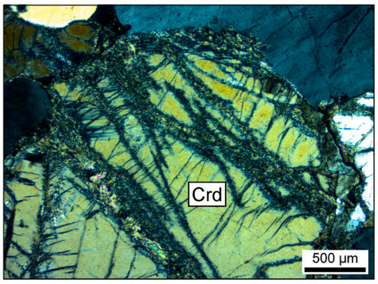

Fig. 5. Summary of the main features of different cordierite-migmatite gneiss samples collected in different localities of the Valpelline Series.

two late systems with different orientations cross-cut each other and the folded S_2 (Fig. 6h and i), striking NW–SE and NNW–SSE (Fig. 7h and i), both with dip angles ranging approximately from 65° to 85° (Fig. 7i). Moreover, some of these late dykes are also affected by open folds (Fig. 6h). Cross-cut relationships visible on the field highlight that aplites and pegmatites striking NW–SE (red dotted line in Fig. 6i) have been emplaced after those striking NNW–SSE (yellow dotted line in Fig. 6i).

5.1.1. *3D virtual-outcrop analysis*

A total number of 369 orientations have been extracted from remote sensing data (Fig. 7): in particular, 25 from UAV-derived point clouds, 107 from LiDAR-derived point clouds both processed in CloudCompare, and 209 from Google Satellite© using the *QgSurf* plug-in within QGIS.

S_1 in basic granulite and brown amphibolite boudins has been traced and measured using the point clouds derived from iPad LiDAR scanning. 32 planes have been extracted (black dots in Fig. 7b). The extracted surfaces have a dip direction both toward S–SE and N–NE. The first

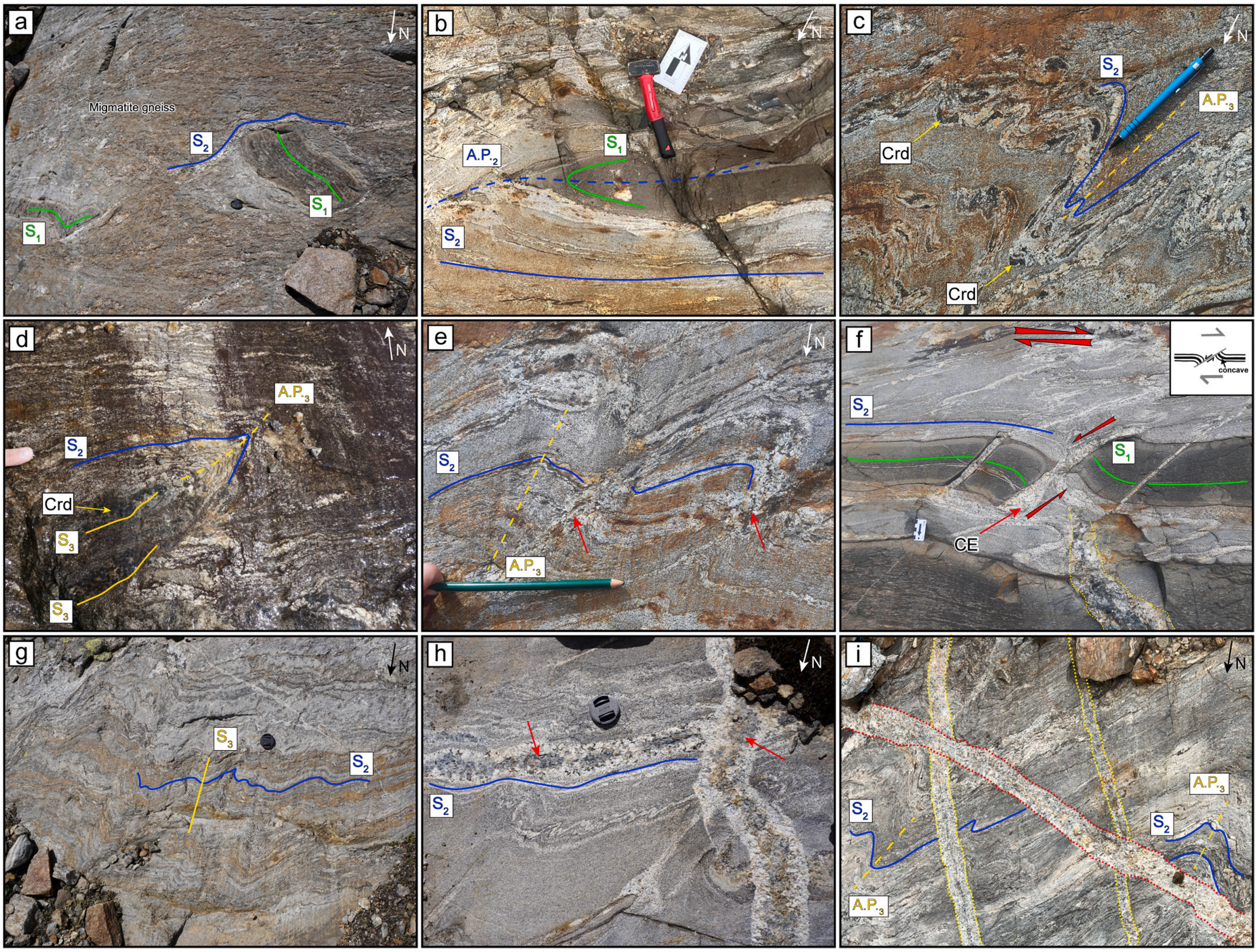

Fig. 6. (a) S_1 foliation in a basic granulite level discordant respect to the external S_2 pervasive in migmatite gneiss; (b) isoclinal F_2 affecting a brown amphibolite level; (c) isoclinal F_3 folds in cordierite-migmatite gneiss; cordierite is folded and concentrated in fold hinges; (d) isoclinal F_3 folds in cordierite-migmatite gneiss with local development of S_3 axial plane foliation made of sillimanite and biotite, wrapping cordierite blasts; (e) asymmetric F_3 folds suggesting shearing of the short limb and injection of melt along it (red arrows); (f) sheared brown amphibolite level developing an "a-type" flanking structure with leucosome as CE element; the sketch of the structure in the upper right side is from Grasemann et al. (2003); (g) S_3 crenulation cleavage in migmatite gneiss; (h) two pegmatitic dykes within migmatite (red arrows): the first is parallel to the S_2, the second cross-cut the S_2 and is gently folded; (i) two systems of pegmatitic dykes cross-cutting F_3 folds. (For interpretation of the references to colour in this figure legend, the reader is referred to the Web version of this article.)

extracted cluster has a dip direction ranging from ~150° to ~190° and dip angles between ~55° and 88°; the second one has a dip direction of ~350° or between ~5° and 20° and two sub-clusters of dip angles, one more sub-vertical and one between ~40° and 65° (Fig. 7b). Planes extracted from the point clouds partially overlap those measured in the field: only the first cluster of orientations dipping toward S–SE is coherent with field measurements (green squares in Fig. 7a). The pervasive foliation S_2 at the outcrop scale has been extracted both from the LiDAR point clouds and the UAV-derived one. The surfaces have a dip direction both toward NE and SE. The first denser cluster has dip directions ranging from ~145° to 195° and dip angles between 20° and 60°; the second one has dip directions between 315° and 360° and dip angles between 0° and 10°, with dip angles similar to the first cluster (Fig. 7d). S_2 orientations extracted from CloudCompare overlap only the cluster dipping toward the S. S_2 orientations extracted from UAV point cloud (black dots in Fig. 7d) partly overlap those from LiDAR and field, but are more scattered, and with relatively lower dip angles. Axes and axial planes related to the D_2 and D_3 folding have not been extracted from CloudCompare due to the relatively low resolution of the point clouds and the 3D outcrop flat shape not permitting line measurements of the axes. For leucosomes discordant to S_2, only strikes have been plotted since the low resolution of the point clouds and the size of the object, the dip angles were scattered or wrong (Fig. 7f).

29 data of aplites and pegmatites directions visible from both the UAV and LiDAR point clouds have been extracted. There are two main clusters of directions: (i) one strikes NW–SE and (ii) the second strikes WNW–ESE (Fig. 7j and k). Minor clusters striking E–W and NE–SW have also been measured from CloudCompare. The data extracted from the *QgSurf* plug-in are more scattered and cover various orientation strikes: the most frequent is the one striking ENE–WSW (Fig. 7l). The data extracted from CloudCompare match better with those measured on the field with the compass.

5.2. Traditional microstructural analysis

Sample VP34 comes from a leucosome-rich portion. It is characterised by a gneissic structure mostly made by pluricentimetric-thick leucocratic levels consisting of plurimillimeter quartz, K-feldspar and cordierite and rare plagioclase alternating with few millimeter-thick sillimanite and biotite-rich melanocratic domains (Fig. 8a).

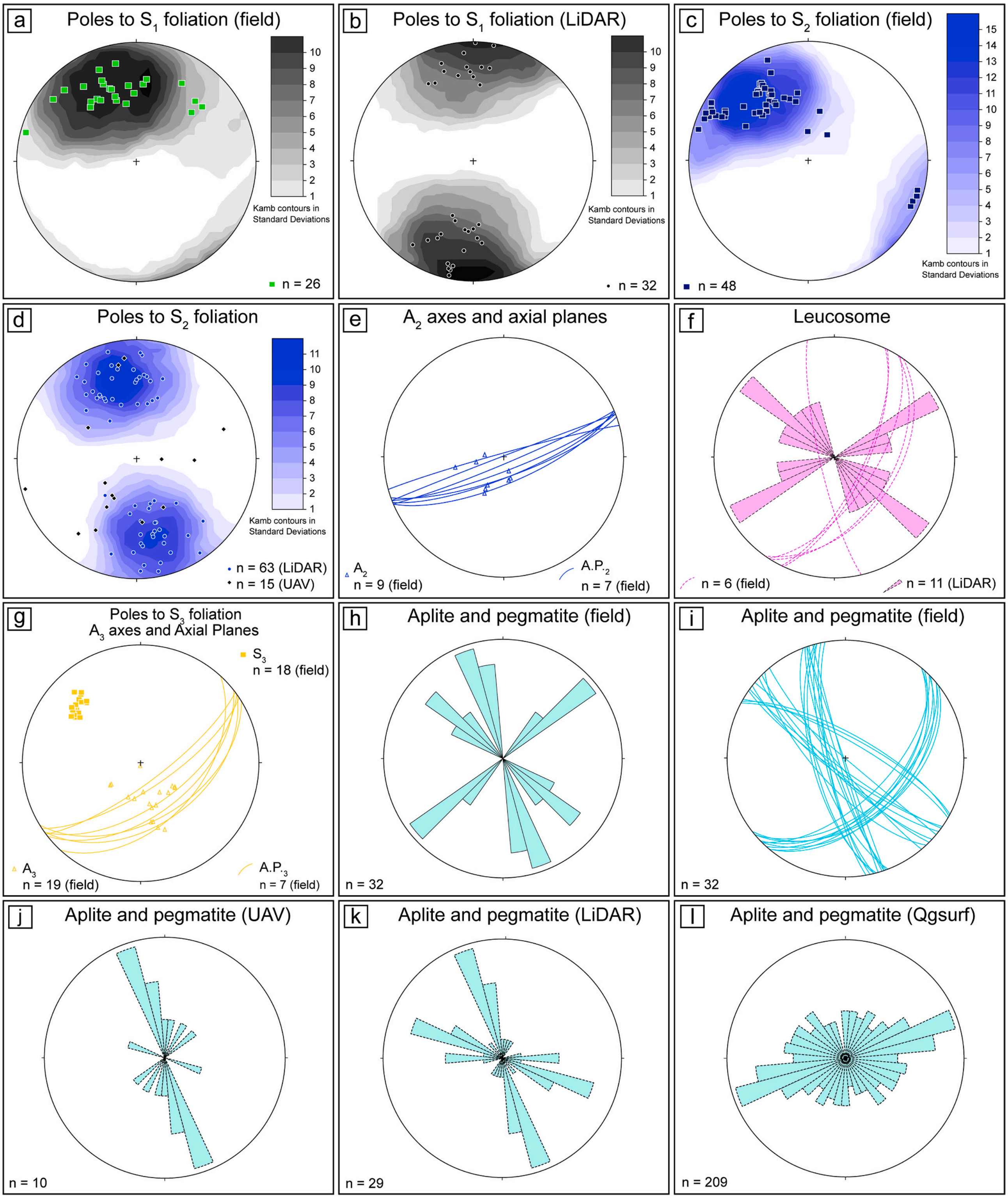

Fig. 7. (a) Equal area stereographic projection (lower hemisphere; made with Stereonet 10; Allmendinger et al., 2013; Cardozo and Allmendinger, 2013) of poles to S_1 foliation manually measured in the field; (b) poles to S_1 foliations measured from LiDAR point clouds; (c) poles to S_2 foliations of field data; (d) poles to S_2 foliations measured from LiDAR point clouds (blue dots with Kamb contour) and from UAV point clouds (black dots); (e) A_2 fold axes (blue triangles) and axial planes (blue planes); (f) projection of leucosomes discordant to the S_2 (planes measured on the field) and strikes of leucosomes obtained from CloudCompare (rose diagrams); (g) poles to S_3 foliations, A_3 axes and axial planes (measured on the field); (h) rose diagrams of the strikes of pegmatitic and aplitic dykes measured on the field; (i) pegmatite and aplites planes measured on the field; (j, k, l) dykes directions extracted from LiDAR, UAV point clouds and Google Earth respectively. (For interpretation of the references to colour in this figure legend, the reader is referred to the Web version of this article.)

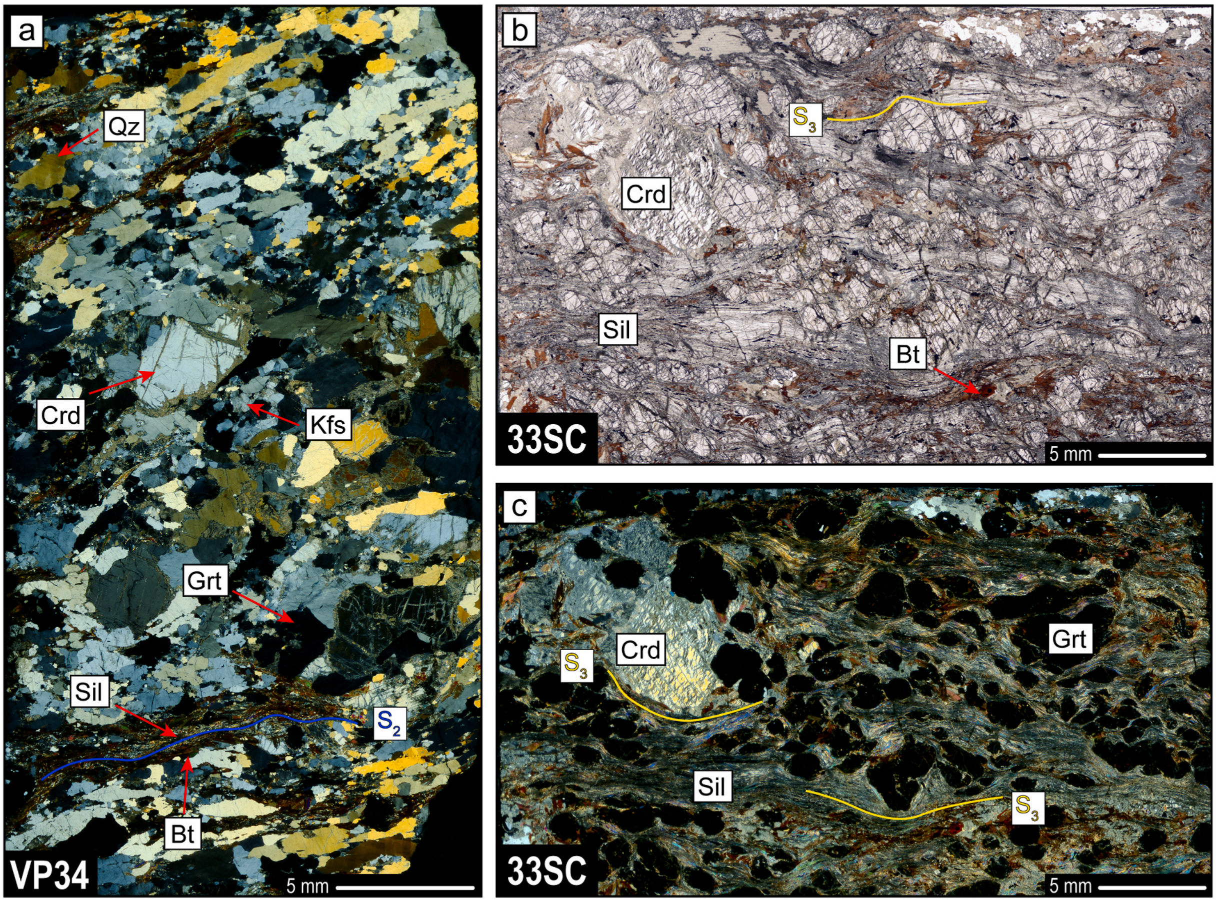

Fig. 8. (a) Thin section scan of the VP34 sample (XPL: crossed-polarized light); (b, c) thin section scans of the 33SC sample (b is PPL: plane-polarized light; c: XPL).

Millimeter-sized garnet porphyroblasts mostly occur in melanosome and in minor amount in leucosome. Cordierite occurs within leucosomes as plurimillimeter-sized porphyroblasts (Fig. 8a). 33SC sample comes from a melanosome and differs from the former for the higher modal abundance of sillimanite, biotite and garnet. In this sample, the pervasive foliation is made by millimeter-sized fibrous and prismatic sillimanite with minor biotite and ilmenite (Fig. 8b and c). Leucosomes are thin, discontinuous and composed of millimeter-sized quartz and minor plagioclase, without K-feldspar (Fig. 8c). Garnet occurs as plurimillimeter-sized and locally flattened porphyroblasts wrapped by the main foliation. In this sample cordierite is mosly plurimillimeter-sized, strongly fractured and locally pseudomorphed by fine white mica aggregates (Fig. 8c).

S_2 is marked by the SPO of sillimanite (Sil II), biotite (Bt II; Fig. 9a and 10) and ilmenite, alternating with leucosomes, made of quartz (Qz II), K-feldpsar and plagioclase in sample VP34 (Fig. 9b). Locally, minor deformations in Bt II crystals along S_2 are observed. Quartz grain size is variable, from plurimillimeter ribbons to millimeter and sub-millimeter equant blasts. Coarse-grained quartz ribbons are oriented marking the S_2 fabric (Fig. 9b). Plagioclase occurs as rare millimeter blasts in the leucosomes of sample VP34 and in discontinuous millimeter-thin levels in sample 33SC, together with quartz. S_2 in sample 33SC is preserved as fold hinges within microlithons of the locally spaced S_3 (Fig. 9c and d). S_3 is well developed in this sample and is marked by sillimanite (Sil III), idiomorphic biotite lamellae (Bt III) and ilmenite, wrapping both garnet and cordierite porphyroblasts (Fig. 9d and e). Garnet in both samples hosts sub-millimeter inclusions of biotite (Bt I), sillimanite (Sil I), and quartz blasts (Qz I), having a rounded shape, thus not in equilibrium with garnet (Fig. 9c, d, f). Locally, sillimanite inclusions align in the rim of the garnet making an internal foliation in continuity with the external S_3 (Fig. 9f). Thus, garnet in sample 33SC grew from pre-to syn-kinematic (Passchier and Trouw, 2005) with respect to S_3. Some of these syn-kinematic garnet porphyroblasts also have a flattened shape (Fig. 8b and c and 9f). Fine-grained aggregates of white mica locally overgrow both cordierite and K-feldspar. Quartz and biotite along S_3 foliation locally make intergrowths after garnet (Qz III and Bt III).

5.2.1. *Quantitative microstructural analysis*

The Mineral-Grain-Size Detector tool (Min-GSD) applied to both samples provided two vectorial grain polygon maps whose grains are labelled with a mineral phase attribute (Fig. 11a and b). As a result, the following rock-forming mineral grains have been distinguished in samples VP34 and 33SC respectively: 1125 and 15058 sillimanite grains, 1275 and 4049 biotite grains, 112 and 1277 garnet grains, 2092 and 757 white mica grains, 560 and 432 cordierite grains, 1086 and 397 plagioclase grains, 86 and 384 ilmenite grains, 1929 and 311 quartz grains; in sample 33SC 127 chlorite grains and 11 rutile grains occur. K-feldspar, detected only in sample VP34, has a number of 2509 grains (Fig. 11a). These values result in different modal percentages, obtained from the Q-XRMA first cycle classification, highlighting huge differences mineral modes (Fig. 11c). Quartz + feldspars (corresponding to leucosome) grains percentage differs in the two samples: in sample VP34 this sum (quartz + K-feldspar + plagioclase) is relatively high (~70%) corresponding to 5524 grains (yellow grains in the right of Fig. 11a); in sample 33SC quartz + plagioclase sum is much lower, corresponding only to ~5% vol with 708 total grains (yellow grains in the bottom of Fig. 11b). Accordingly, biotite + sillimanite grains percentage (corresponding to the melanosome) is higher in sample 33SC (~70%) and lower in VP34 (~10%). The same is for garnet which is more abundant in sample 33SC (Fig. 11c).

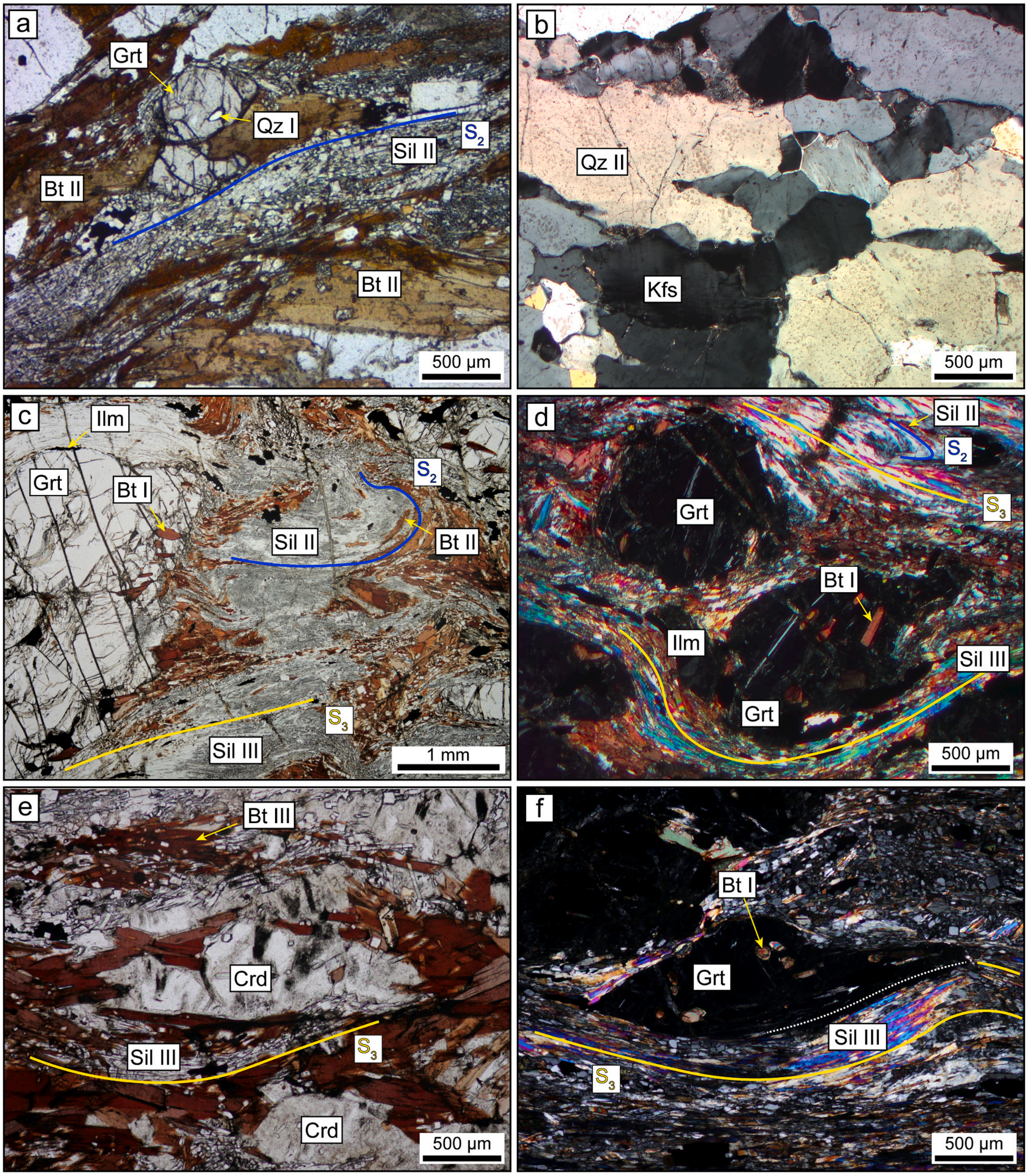

Fig. 9. (a) S_2 foliation in the VP34 sample: the S_2 is marked by Sil II and Bt II (PPL); (b) quartz-feldspathic domain consisting of elongated Qz II and Kfs in the VP34 sample (XPL); (c) S_2 microfold preserved within microlithon, whose limbs are parallel to S_3 foliation consisting of Sil III and Bt III in sample 33SC (PPL); (d) Grt porphyroblasts wrapped by the S_3 foliation (XPL); (e) S_3 made of Sil III and Bt III wrapping Crd blasts (XPL); (f) syn-kinematic (to S_3) flattened Grt porphyroblast wrapped by the S_3 foliation, showing an internal foliation in the rim concordant with the external S_3, made of sillimanite (XPL).

Grain orientations data have been extracted from each mineral phase to check whether a link between their orientations and the foliation they mark occurs. In particular, the MFA calculates the long axis orientation angle (0–180°) measured clockwise from a reference vertical axis. The long axis orientation values are clustered at ~90° for biotite, sillimanite, ilmenite and quartz (Fig. 12a). In detail, biotite, sillimanite and ilmenite long axis orientations mostly have values of ~90°, with two minor clusters at ~60° and ~120° for both samples. In sample VP34, all phases also show a pronounced cluster between 60° and 90°, reflecting the local anastomosed geometry of S_2 foliation. There is a relatively small number of grains with long axis orientation at 0° or 180°, and these occurrences are more common in the sample 33SC. Garnet orientations have been plotted only for sample 33SC, where, despite exhibiting more dispersion compared to other mineral phases, they show a weak clustering of orientations at ~90° (Fig. 12a). Similarly, this pattern emerges for K-feldspar found exclusively in sample VP34, where a slight clustering around 90° is observed (Fig. 12a).

The long axis orientation data is easily observed through orientation maps extracted from ArcGIS (Fig. 12b, c, d, e, f, g). S_2 in sample VP34 is defined by the sillimanite and biotite grains whose long axes have orientations between ~60° and 110° (Fig. 12b and c). Quartz and K-feldspar long axis orientations in the leucosome, with angles comprised

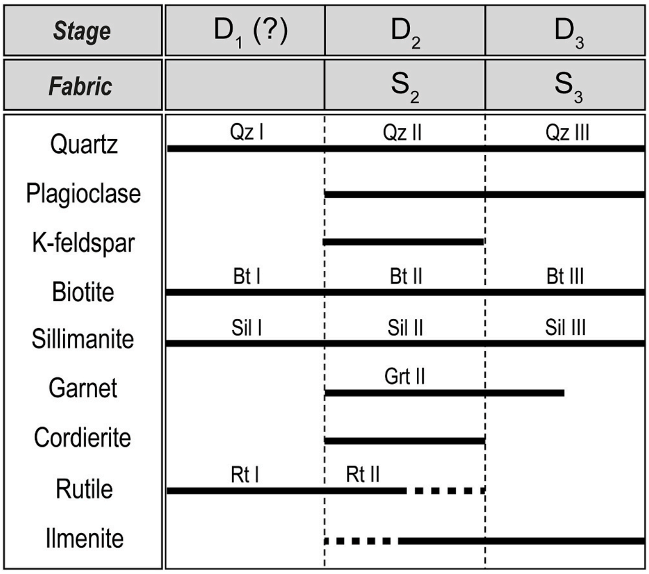

Fig. 10. Blastesis vs. deformation diagram of cordierite-migmatite gneiss.

between ~60° and 110° (light blue and yellowish shades; Fig. 12d and e), also support S_2.

Looking at sillimanite long axis orientation maps for sample 33SC (as already shown in Caso, 2023), the grains having orientation at ~ 90° are those marking the main S_3 foliation (Fig. 12f and g). Grains having various orientations, such as 0–30° (light-blue shades) or 130–180° (reddish shades; Fig. 12f and g) mark S_2 in the microlithons (see zoom rose diagram and map in Fig. 12g). Also, some of more scattered orientations not directly correlated with S_2 may be represented by grains included within garnet.

Quartz and K-feldspars grains locally show SPO in sample VP34, marking S_2 foliation. This is constrained through the roundness parameter (calculated as the width/lenght ratio of each grain) of these two mineral phases (Fig. 13a and b). Quartz marking S_2 corresponds to grains with roundness between 0.19 and 0.53 (yellow-orange grains in Fig. 13a). Purple and blue grains correspond to those whose roundness is closer to 1 and are not suitable for marking S_2 (Fig. 13b and c). As shown in the rose diagram for sample 33SC, a huge number of garnet grains has long axis with orientation at ~90° (Fig. 12a), parallel to the main S_3 foliation (yellow, green, and orange grains in Fig. 13d). In this case, the roundness parameter of garnet is often lower than 1 (yellow to orange grains; Fig. 13e and f). This is in accordance with the flattened shape of

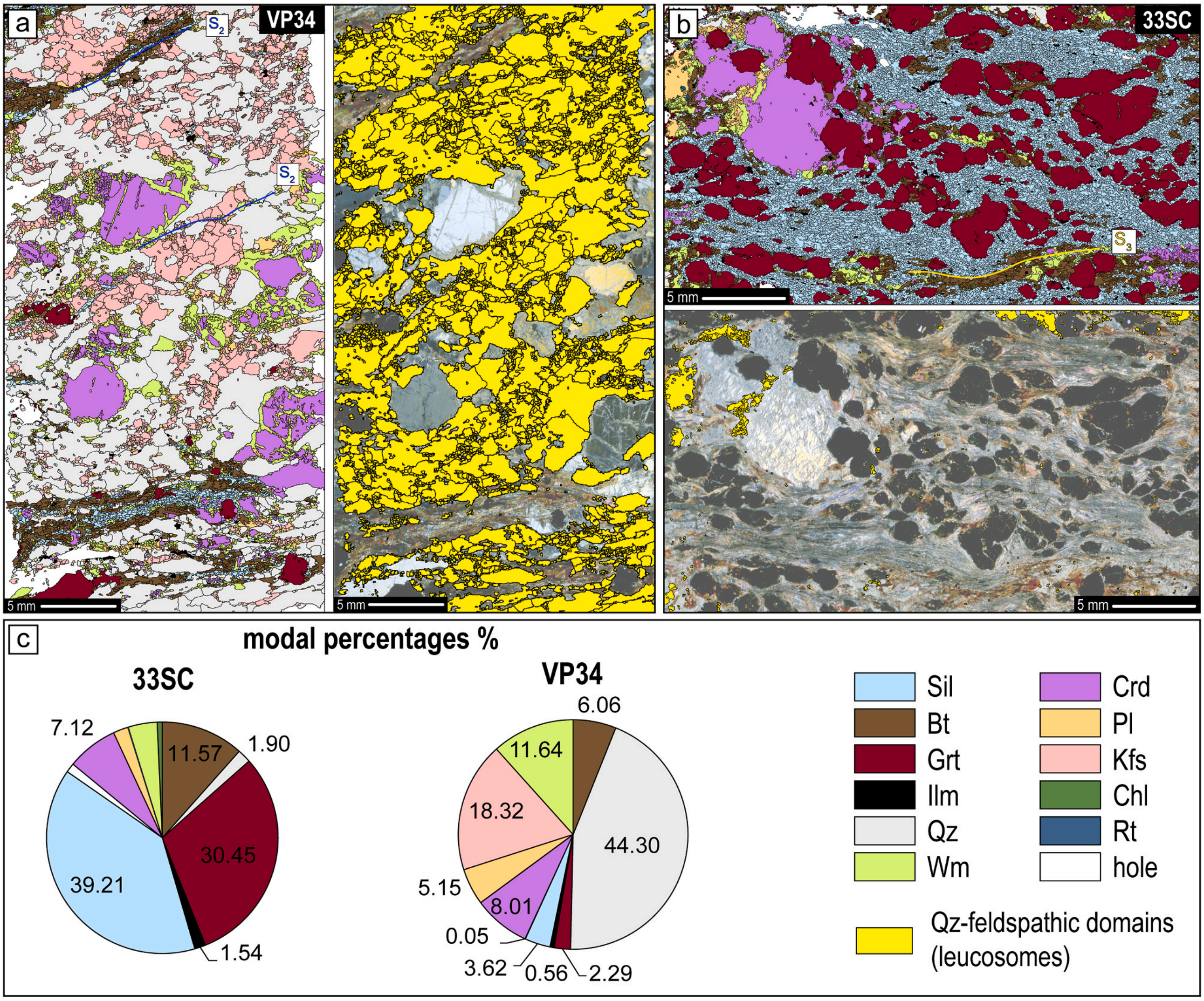

Fig. 11. (a, b) Mineral grain maps of the samples 33SC and VP34 respectively, obtained from the MFA toolbox; maps highlighting quartz-feldspathic domains in yellow are reported at the right and at the bottom respectively; (c) modal percentages of both samples obtained from the first cycle of Q-XRMA. (For interpretation of the references to colour in this figure legend, the reader is referred to the Web version of this article.)

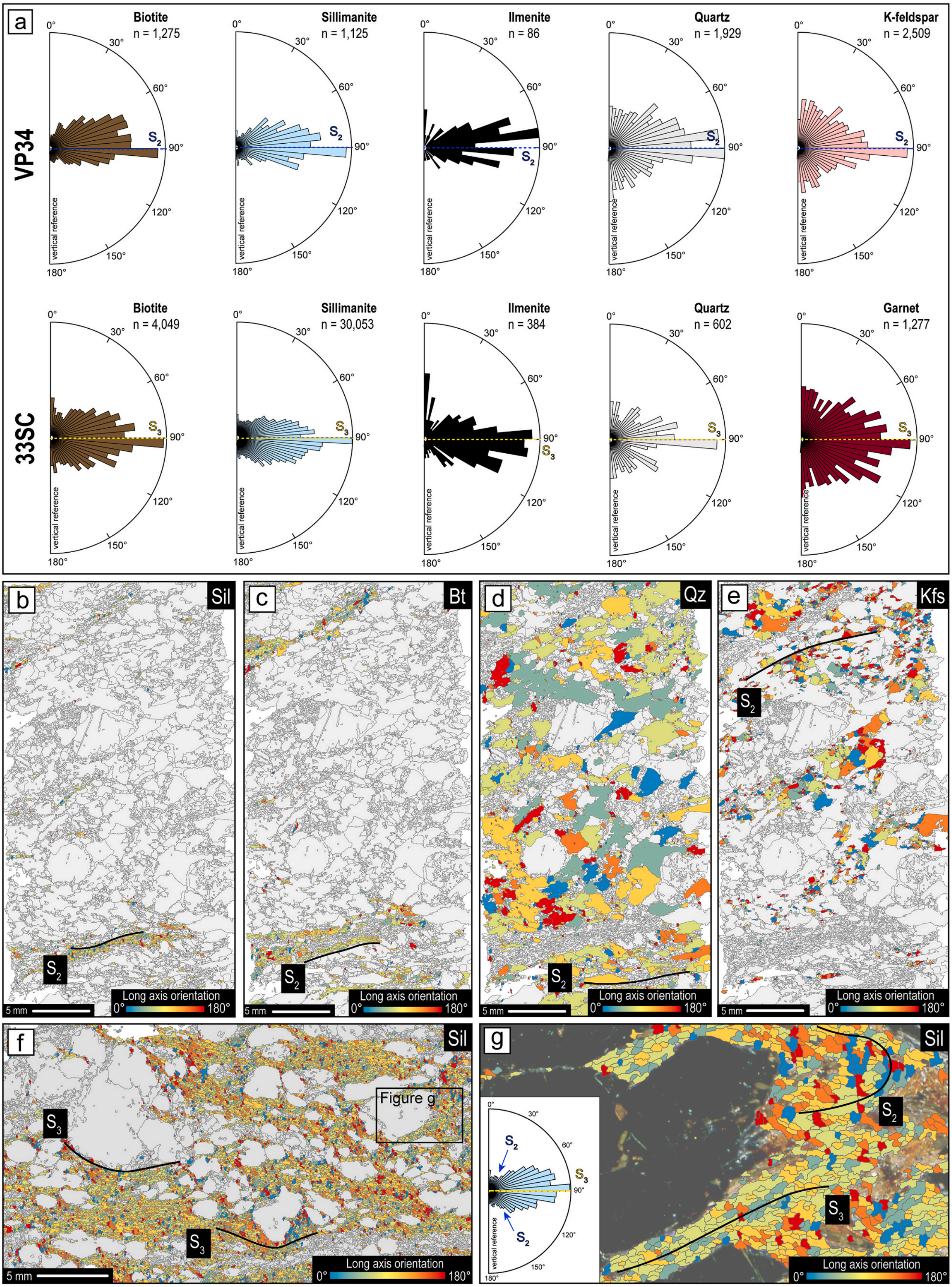

Fig. 12. (a) Long axis orientation rose diagrams for the main phases occurring in the two analysed samples; (b, c, d, e) long axis orientations maps of sillimanite, biotite, quartz and K-feldspar in sample VP34; f) long axis orientation map of sillimanite in sample 33SC (modified from Caso, 2023); (g) detail of figure f, showing a microdomains where the overprinting relationship between S_2 and S_3 are visible from long axis sillimanite orientation; in the bottom left the rose diagram shows data only of this zoom.

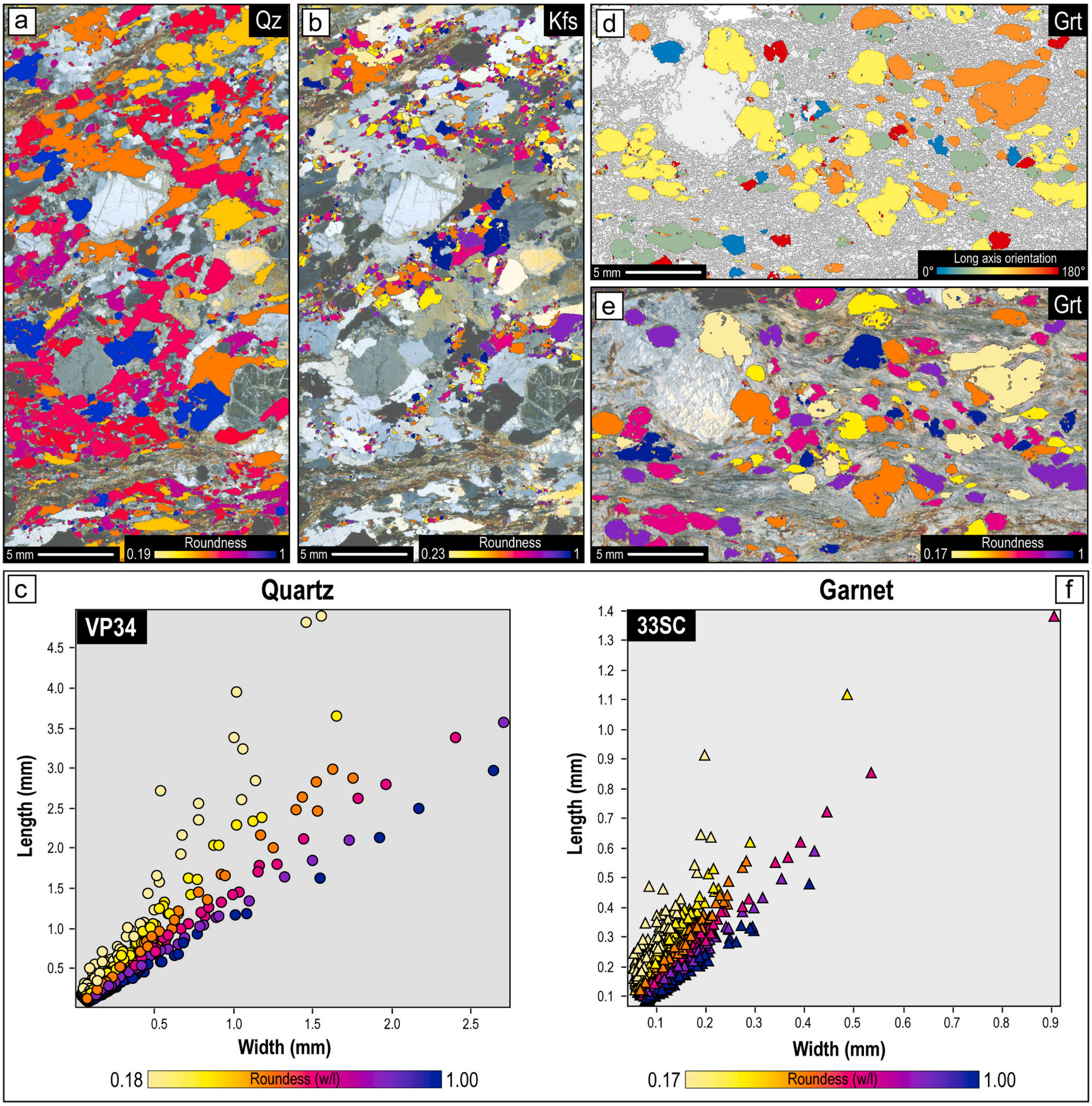

Fig. 13. (a, b) Roundness map of quartz and K-feldspar in sample VP34; (c) width/length ratio (roundness) of quartz grains in the sample VP34; (d) long axis orientation map of garnet grains in the sample 33SC; (e) roundness map of garnet in sample 33SC; (f) width/length ratio (roundness) of garnet grains in the sample 33SC.

the grains, making them suitable for marking S_3 foliation (Fig. 13e and f).

6. Quantitative mineral-chemical analysis

Mineral-chemical analysis on sample 33SC was carried out on biotite and garnet by Caso (2023) using a different software. Here we used the Q-XRMA second cycle to obtain biotite and garnet-calibrated maps, extending the comparison with EMPA point analyses and deeply discussing the results.

Mg, Fe and Ti calibrated maps were analysed to check biotite chemical variations. The Mg content in biotite varies from 2.39 to 3.24 apfu (Fig. 14a). Fe varies from 1.50 to 2.20 apfu (Fig. 14b), resulting in Mg# (Mg/Fe + Mg) from ~0.5 to 0.7 (Fig. 14c). Mg increases toward the core and is higher in the biotite grains in the garnet strain shadows (Fig. 14a). Conversely, Fe is higher in biotite grains included within garnet porphyroblasts, at the rim of the grains marking the S_3 foliation and in biotites replacing cordierite (Fig. 14b). The Ti content ranges from 0.30 to 0.70 apfu (Fig. 14d) and is higher in biotite grains included within garnet (Bt I) and increases in the core of some coarser biotite blasts (Bt II). The lowest values are found in some biotites marking the main S_3 foliation (Bt III), especially in those growing after cordierite (Fig. 14d).

The Ti content of biotite has been used for calculating the temperatures through the Ti-in-biotite thermometer of Henry et al. (2005). Considering only EMPA point mineral-chemical data (pink symbols in

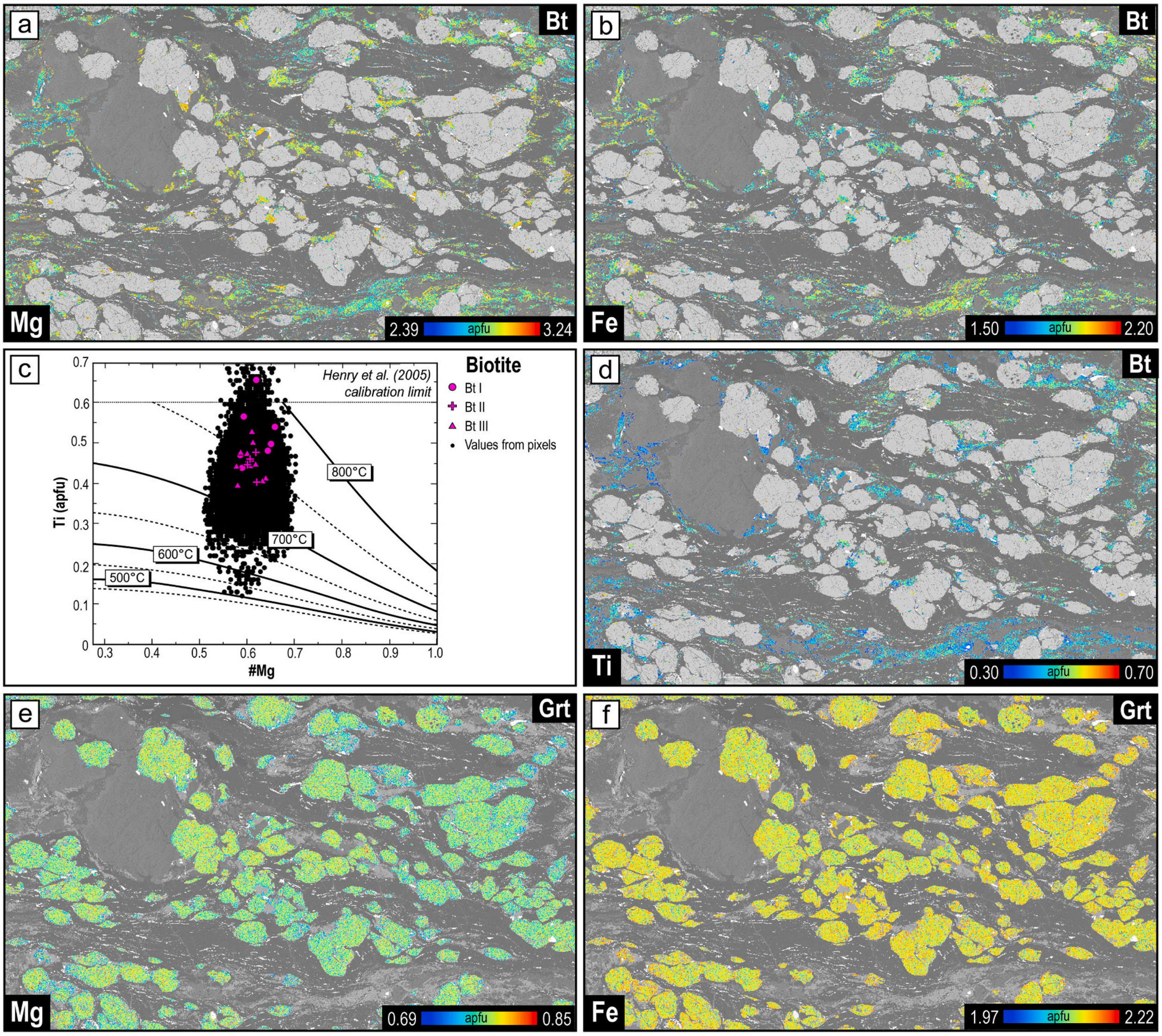

Fig. 14. (a) Mg apfu calibrated map of biotite; (b) Fe apfu calibrated map of biotite; (c) #Mg vs Ti apfu data of biotite extracted from each pixel of the calibrated map (black dots) and EMPA analyses (discriminated on their microstructural positions) used for calibration with Q-XRMA (pink symbols); (d) Ti apfu calibrated map of biotite; (e) Mg apfu calibrated map of garnet; (f) Fe apfu calibrated map of garnet. (For interpretation of the references to colour in this figure legend, the reader is referred to the Web version of this article.)

Fig. 14c), the *T* ranges between 730 and 800 °C; using Ti content extracted from each pixel of the calibrated map, the *T* range becomes wider, with a mean cluster between 650 and 800 °C.

Garnet has already described in Caso (2023) and is mostly homogeneous. It shows only a weak zonation for Ca, thus with increasing grossular component toward the rim. Mg and Fe apfu, as visible from calibrated maps, are homogeneous with a slight variation toward the rim, especially when in contact with biotite (Fig. 14e and f). Mg is mostly between 0.77 and 0.80 apfu, up to decreasing at 0.69 in the rim in contact with biotite (Fig. 14e). Fe is homogeneous in most of the blasts, being 2.13 apfu, up to 2.22 in the rim in contact with biotite (Fig. 14f). All chemical data obtained by the EMPA and extracted from each pixel of the calibrated maps are reported in Supplementary Material 2.

7. Discussions

7.1. *Tectono-metamorphic evolution of the Valpelline Series*

The multiscale and multi-method structural analysis allowed the definition of three tectono-metamorphic stages in the Valpelline Series, namely D_1, D_2 and D_3 (Fig. 15).

D_1 is testified by the S_1 foliation, preserved mostly in basic granulite and brown amphibolite boudins and locally discordant to the external S_2 (Fig. 6a and b and 15). S_1 dips mainly toward the SW with scattered dip angles. At the microscale, in metabasic rocks, this foliation is defined by the alignment of clino- and orthopyroxene, brown amphibole, plagioclase and in minor amounts biotite and orthoamphibole (see Caso et al., 2024 for details about D_1). In migmatite gneiss is harder to constrain the D_1: the round-shaped inclusions of Bt I, Sil I, and Qz I within garnet or cordierite may be both remnants of the D_1 stage in the hosting migmatitic gneiss or just inclusions from the D_2 stage.

Extracted quantitative parameters for the rock-forming mineral phases support the above-described relationships: part of biotite, sillimanite and quartz grains with long-axis orientations diverging from the main foliation (Fig. 12a) can be ascribed to Bt I, Sil I and Qz I grains included within garnet and cordierite which show no preferred orientation. Nevertheless, this parameter alone is not sufficient for this constrain; most of these grains have a round shape, rarely elongated, corresponding to grains with roundness (w/l) parameter closer to 1 (e.g., quartz data in purple and blue in Fig. 13c). Mineral-chemical variations

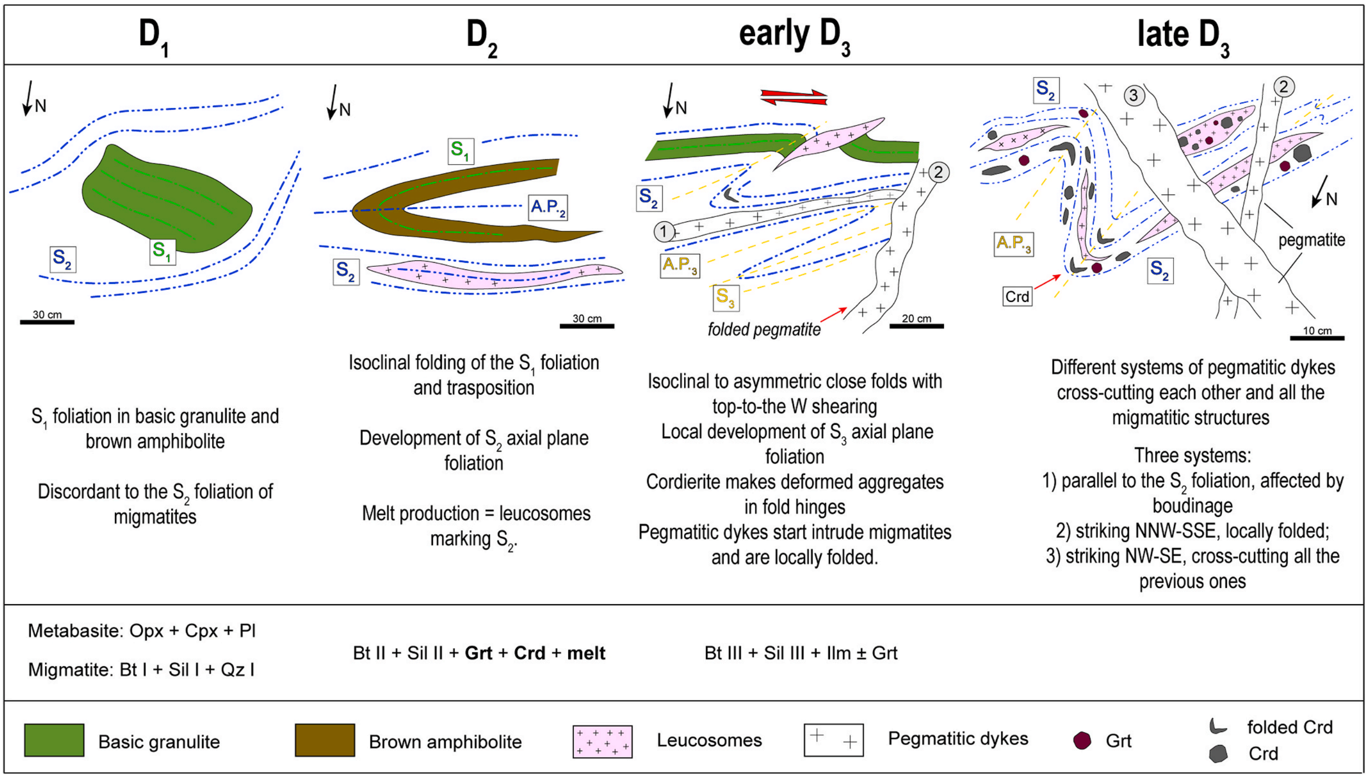

D_1	D_2	early D_3	late D_3
S_1 foliation in basic granulite and brown amphibolite Discordant to the S_2 foliation of migmatites	Isoclinal folding of the S_1 foliation and trasposition Development of S_2 axial plane foliation Melt production = leucosomes marking S_2.	Isoclinal to asymmetric close folds with top-to-the W shearing Local development of S_3 axial plane foliation Cordierite makes deformed aggregates in fold hinges Pegmatitic dykes start intrude migmatites and are locally folded.	Different systems of pegmatitic dykes cross-cutting each other and all the migmatitic structures Three systems: 1) parallel to the S_2 foliation, affected by boudinage 2) striking NNW-SSE, locally folded; 3) striking NW-SE, cross-cutting all the previous ones
Metabasite: Opx + Cpx + Pl Migmatite: Bt I + Sil I + Qz I	Bt II + Sil II + **Grt** + **Crd** + **melt**	Bt III + Sil III + Ilm ± Grt	

Fig. 15. Synoptic table summarizing the main features of the tectono-metamorphic stages defined in the Valpelline Series.

are not strongly enough to constrain these relationships, since HT metamorphism often led to chemical homogenisation during cooling. However, only Bt I included within garnet locally preserves chemical variation, thus being characterised by the highest Ti values (0.5–0.7 apfu; Fig. 14c and d), resulting in higher calculated temperatures up to ~800 °C (Fig. 14d).

During this stage S_1 is deformed and S_2 axial plane foliation develops. S_2 is characterised by the alternation between melanosomes and leucosomes within migmatite gneisses. S_2 dips toward the SW, with high dip angles. At the microscale, S_2 is well-developed in sample VP34 and is highlighted by SPO of sillimanite and biotite (Sil II and Bt II) in the melanosomes and SPO of quartz (Qz II) and K-feldspar in the leucosomes. Quartz grains highlighting S_2 in sample VP34 (Qz II) are those having a relatively low roundness parameter, due to their elongated shape (Fig. 13a–c). The long axis orientations with a main cluster oriented at ~90°, extracted through the MFA tool for these mineral phases highlight S_2. Long axis orientations at 30° and 120° support the presence of Bt II highlighting the remnants of the S_2 within the microlithons of sample 33SC. Locally within these domains, larger deformed Bt II grains show a relatively high-Ti content (~0.5–0.7 apfu; Fig. 14c and d).

Leucosome percentage (quartz + plagioclase + K-feldspar), estimated at the microscale through the MFA, may give an idea of the amount of melt present within the studied rock volume, in this case higher in sample VP34 (Fig. 11a). However, leucosome does not always represent the melt-fraction (e.g., Lee et al., 2020) or it can easily escape during brittle or shear deformation (Sawyer, 2001; Etheridge et al., 2021; Daczko and Piazolo, 2022). Moreover, it can also be possible that some of the K-feldspar or plagioclase blasts occurring within leucosomes represent solid peritectic products of biotite-dehydration melting reaction (Le Breton and Thompson, 1988; Spear, 1994; Waters, 2001; White et al., 2014) and not always something crystallised directly from the melt. Nevertheless, in these samples and in others of the VP, several melt-bearing microstructures have been recognised (Caso et al., 2024), such as melt films among grain boundaries or back-reaction structures after melt consumption (e.g., biotite-quartz intergrowths; Sawyer, 2008; Kreigsman and Alvarez-Valero, 2010), related to the D_2-D_3 stages. It is harder to estimate how much melt has been produced in sample 33SC: this may represent a situation where most of melt has escaped from the rock volume or has been consumed during back-reaction involving peritectic phases and melt, producing biotite and sillimanite.

Garnet and cordierite, which occur within leucosomes formed during D_2, represent peritectic phases, according to the Bt + Sil + Qz + Pl = Grt + Crd + Kfs + melt reaction (Kreigsman and Alvarez-Valero, 2010; Waters, 2001; White et al., 2014). The mutual relationship between garnet and cordierite is not easy to constrain; however, both are wrapped by S_3 sillimanite-biotite foliation, constraining their growth during the D_2 (see also Caso et al., 2024).

Garnet growth relations during the partial melting evolution are difficult to reconstruct using mineral-chemical criteria; these are homogenous and show almost no chemical zoning, apart from weak zoning of Fe and Mg toward the edge in contact with biotite, due to late diffusional resetting during cooling. This is also testified by temperatures obtained in these rocks using the Grt-Bt exchange thermometer: temperatures go down to 650 °C (Caso et al., 2024).

During D_3, S_2 is deformed with open to isoclinal folds, with the local development of the sillimanite-rich S_3 foliation (Fig. 6c, d, e, f and 15). During this stage, leucosomes and cordierite are deformed. This is more evident at the mesoscale, where dark-grey aggregates of cordierite are folded and concentrated in the fold hinges (Fig. 6d and 15).

At the microscale, S_3 is well observable in sample 33SC and it is marked by the SPO of sillimanite and biotite. The long axis orientations with a main cluster oriented at ~90°, extracted from MFA tool for sillimanite, biotite, and ilmenite refer to S_3 (i.e., Sil III and Bt III). Even though garnet grows during D_2 it continues its crystallisation during the early D_3. Quantitative MFA data of garnet demonstrate the presence of flattened porphyroblasts corresponding to those having a roundness locally strongly <1 (Fig. 13e and f). Bt III corresponds to grains having a lower Ti content with respect to Bt I and Bt II, ranging from ~0.3 to 0.5 apfu and thus yielding slightly lower temperatures between ~650 and 730 °C (Fig. 14d).

The two analysed samples are representative of different stages of the partial melting history of the VP: indeed, sample VP34, which corresponds to a cordierite-bearing leucosome (Fig. 12a), is representative of melt production during D_2, since its main foliation corresponds to S_2. Conversely, sample 33SC is almost devoid of leucosomes, apart from rare millimeter-thin levels, and is strongly enriched in sillimanite and biotite that mark S_3 foliation, with S_2 preserved in few microdomains as relict fold hinges. Thus, this sample may represent the melt-consuming reactions during D_3, where such a high modal amount of sillimanite can be produced by garnet or cordierite back-reacting with melt, giving Sil III and Bt III (Spear, 1994; Kreigsman and Alvarez-Valero, 2010). Meanwhile, is also possible that part of melt has escaped from this rock during D_3, migrating toward low-strain zones.

Geometrical overprinting relationships between different systems of aplite and pegmatite dykes, which widely intrude into the migmatite gneiss, allowed to divide the D_3 into an early and late D_3 stage (Fig. 15). One system of dykes parallel to the S_2 and locally affected by boudinage (Fig. 6h) may have intruded gneiss during the D_2 or early D_3 stage. Then, other systems of dykes intruded migmatites by cross-cutting the syn-D_2 and syn-D_3 foliations and folds (Fig. 6h and i). Moreover, part of these dykes cross-cutting D_3 folds, and striking NNW-SSE are also locally affected by open folds (Fig. 6h), probably developed during the ongoing deformation during early D_3 (Fig. 15). It is possible that dykes started intruding migmatites during late stages of D_2, using the S_2 foliation as preferential path or weakness layer, being progressively affected by boudinage during progressive deformation; then, during D_3 folding, some intruding dykes are folded. In the latest stages of D_3, dykes intruded migmatite gneiss, crosscutting all structures ($D_2 + D_3$) without being further deformed.

7.2. Pros and cons of quantitative multiscale structural analysis

The multiscale digital acquisition methods used in this work have given an interdependent picture of the reconstructed sequence of deformation events (Fig. 15). This allowed also to better constrain the paragenetic sequence on which the thermodynamic calculations are usually based (Palin et al., 2016).

In particular, the quantitative mesoscale structural analysis made by the integration of traditional compass measurements with data extracted from LiDAR sensor or UAVs-derived point clouds, allowed to collect a statistically high number of structural data (in most cases more than ~50), even from inaccessible outcrop portions. Nevertheless, there are still some structural artefacts resulting from the use of CloudCompare on point clouds. In this case, the problems were eliminated by the direct ground control carried out during the traditional survey campaign (i.e., comparison with compass manual measurements of structural elements). Indeed, even though most of the S_1 and S_2 data extracted from CloudCompare fit well with the ones measured on the field (see Fig. 7a, b, c, d, b), this software often extracts orientations having the same strike as those measured with the compass, but with opposite dip directions. This can be explained by a difference in the dip angle of a few degrees (5–10°) which apparently changes the dip direction of sub-vertical planes. However, this misfit may derive from systematic errors during field-based data collecting, especially of sub-vertical planes where the user is often led to make the planes dip toward the same direction. Moreover, as is often the case, these artefacts can be also caused by: a) the low density of the point clouds useful for reconstructing the 3D model; b) the presence of shadows during LiDAR or UAVs acquisitions; c) flattened outcrop exposure leading to wrong plane interpolation and measure; d) the difficulty of acquiring data in places that are too inaccessible leading to a low number of data to be used as ground control. Although the technique still has some problems to overcome, it should be able to integrate perfectly with the traditional methods used to date. Data extracted measuring the orientations of dykes polylines traced on Google Satellite© in QGIS, are the most scattered. This dispersion probably derived from artefacts and "holes" of the DEM itself, used by the *QgSurf* plug-in to measure dip directions and dip of a plane interpolated from the traced polyline. This problem should be overcome in two ways: (i) using a higher resolution DEM, better though extracted from UAVs survey which can have resolutions of few centimeters; (ii) by carefully excluding orientations without a geological meaning, using manual data as ground control. Nevertheless, this technique has the advantage of being low-cost, since Google Satellite© and QGIS tools are freely available and do not require expensive hardware to be used.

On the other hand, also conventional structural analysis, characterised by the manual collection of structural data, is a process which may be susceptible to human errors and biases. Therefore, to obtain an objective structural assessment, the integration of traditional methods and semi-automated techniques is necessary to have a double-check of structural measurements and quantitively constrain the polyphase deformation.

The possibility of storing vectorised, microstructure-derived large datasets subdivided by mineral phase through the MFA toolbox, opens up the possibility of following the path of a true digital transition of geo-petrostructural data system acquisition, possibly within a unique and interoperable geological large data system (georeferenced GIS databases). However, these data may still be somewhat cumbersome to obtain since it is necessary to acquire EMPA X-ray maps with adequate resolution, resulting in high costs and time-consuming grain post-processing.

Nevertheless, these digital storing of microstructural data will open the possibility of better interoperate with previously available datasets, allowing them to be integrated synergistically in a broader sense.

8. Conclusions

This work described a multiscale approach that combines traditional field-based methods with remote-sensing and quantitative techniques useful to investigate crystalline basements. In particular, we have integrated traditional structural survey with the extraction of structural data from LiDAR and UAVs-derived point clouds, and Google Satellite©. Using the point clouds and Google Satellite© imagery, we extracted structural data also from steep inaccessible outcrop portions, extending the observation scale. This allowed for increasing the number of the main structural element orientations (foliations, leucosomes and dykes), using the manual field compass data as ground control. Traditional microstructural analysis was combined with the extraction of quantitative shape parameters from semi-automated grain digitisation, stored in a GIS database, allowing to constrain the structural evolution.

The provided quantitative multiscale structural analysis allowed the reconstruction of the tectono-metamorphic evolution of the migmatitic rocks in the Valpelline Series. In particular, three main tectono-metamorphic stages have been recognised, referred to the H*T* evolution of the VP crust during the Permian. D_1 is a solid-state tectono-metamorphic stage, testified by the S_1 foliation preserved in basic granulite and brown amphibolite boudins. D_2 is related to melt production and development of the regional S_2 foliation, garnet, and cordierite growth; early D_3 is characterised by folding of the S_2 and local development of S_3 sillimanite-rich melt-consuming foliation wrapping around garnet and cordierite porphyroblasts. Lastly, three systems of aplites and pegmatites intrude within migmatitic gneiss from early-to late D_3-stages, cross-cutting all the migmatitic structures.

The integration of traditional and innovative multiscale structural analysis has proven to be an efficient approach to ease the study of migmatitic crystalline basements, characterised by complex superimposed structures and different metamorphic assemblages.

CRediT authorship contribution statement

F. Caso: Conceptualization, Data curation, Formal analysis, Investigation, Methodology, Validation, Visualization, Writing – original draft. **C.B. Piloni:** Data curation, Investigation, Writing – review &

editing. **M. Filippi:** Supervision, Writing – review & editing. **A. Pezzotta:** Data curation, Investigation, Methodology, Writing – review & editing. **E. Fazio:** Investigation, Supervision, Writing – review & editing. **R. Visalli:** Supervision, Writing – review & editing. **G. Ortolano:** Supervision, Writing – review & editing. **M. Roda:** Funding acquisition, Project administration, Supervision, Writing – review & editing. **M. Zucali:** Conceptualization, Funding acquisition, Investigation, Project administration, Writing – review & editing.

Declaration of competing interest

The authors declare that they have no competing financial interests or personal relationships that could have appeared to influence the work reported in this paper.

Data availability

Data will be made available on request.

Acknowledgements

We thank two anonimous reviewers the editor F. Agosta for their useful suggestions. This research has been funded by "PSR2020_MRODA". The results here presented have been developed in the frame of the MIUR Project "Dipartimenti di Eccellenza 2017—Le Geoscienze per la società: risorse e loro evoluzione (work package 3, tasks 3.3 and 3.4)". The work was partly supported by the Italian Ministry for Universities and Research (MUR) through the project "Dipartimenti di Eccellenza 2023–27".

Appendix A. Supplementary data

Supplementary data to this article can be found online at https://doi.org/10.1016/j.jsg.2024.105099.

References

Agisoft Metashape. 2024. Available online: http://www.agisoft.com/downloads/installer/. (accessed 21.03.24.).

Allmendinger, R.W., Cardozo, N.C., Fisher, D., 2013. Structural Geology Algorithms: Vectors & Tensors. Cambridge University Press, Cambridge, England.

Angiboust, S., Glodny, J., Oncken, O., Chopin, C., 2014. In search of transient subduction interfaces in the dent blanche–sesia tectonic system (W. Alps). Lithos 205, 298–321. https://doi.org/10.1016/j.lithos.2014.07.001.

Angrand, P., Mouthereau, F., 2021. Evolution of the Alpine orogenic belts in the Western Mediterranean region as resolved by the kinematics of the Europe-Africa diffuse plate boundary. BSGF-Earth Sci. Bull. 192 (1), 42. https://doi.org/10.1051/bsgf/2021031.

Ashworth, J.R., 1985. Migmatites. Blackie & Son Limited), Glasgow and London.

Beltrando, M., Compagnoni, R., Lombardo, B., 2010. (Ultra-) High-pressure metamorphism and orogenesis: an Alpine perspective. Gondwana Res. 18, 147–166. https://doi.org/10.1016/j.gr.2010.01.009.

Bonasera, M., Cerrone, C., Caso, F., Lanza, S., Fubelli, G., Randazzo, G., 2022. Geomorphological and structural assessment of the coastal area of capo faro promontory, NE salina (aeolian islands, Italy). Land 1 (7), 1106. https://doi.org/10.3390/land11071106.

Bonasera, M., Petroccia, A., Caso, F., Cerrone, C., Gregorio, F., 2023. Integrated geomorphological and structural analysis of coastal cliffs: the case study of Capo Faro Promontory, NE Salina, Aeolian Islands, Italy. In: 2023 IEEE International Workshop on Metrology for the Sea; Learning to Measure Sea Health Parameters, MetroSea 2023 - Proceedings, 2023, pp. 519–523. https://doi.org/10.1109/MetroSea58055.2023.10317191.

Brandolini, F., Cremaschi, M., Zerboni, A., Degli Esposti, M., Mariani, G.S., Lischi, S., 2020. SfM-photogrammetry for fast recording of archaeological features in remote areas. In: Bagnasco, G., Bortolotto, S., Garzulino, A., Marzullo, M. (Eds.), Milano internazionale: la fragilità territoriale dei contesti archeologici. Atti del Convegno Internazionale (Milano, 13 marzo 2019), «Archeologia e Calcolatori», pp. 33–45. https://doi.org/10.19282/ac.31.2.2020.04, 31.2.

Brown, M., 1973. The definition of metatexis, diatexis and migmatite. PGA (Proc. Geol. Assoc.) 84, 371–382. https://doi.org/10.1016/S0016-7878(73)80021-5.

Cardozo, N., Allmendinger, R.W., 2013. Spherical projections with OSXStereonet. Comput. Geosci. 51, 193–205. https://doi.org/10.1016/j.cageo.2012.07.021.

Caso, F., 2023. Quantitative combined multiscale structural and minero-chemical analysis to unravel the tectono-metamorphic evolution of cordierite-migmatite gneiss from the Valpelline Unit (Dent-Blanche Nappe, Western Italian Alps, Valle d'Aosta). Rend. Online Soc. Geol. It. 60, 2–10. https://doi.org/10.3301/ROL.2023.20.

Caso, F., Strambini, A., Zucali, M., 2024. Structural, lithostratigraphic and thermal features of a permian lower crust from the western Italian Alps (valpelline series, valle d'Aosta). Geol. Mag. https://doi.org/10.1017/S0016756824000037 (in press).

Cawood, A.J., Bond, C.E., Howell, J.A., Butler, R.W.H., Totake, Y., 2017. LiDAR, UAV or compass-clinometer? Accuracy, coverage and the effects on structural models. J. Struct. Geol. 98, 67–82. https://doi.org/10.1016/j.jsg.2017.04.004.

CloudCompare. 2024. Available online: https://cloudcompare-org.danielgm.net/release/. (accessed 21.03.24.).

Corti, L., Zucali, M., Visalli, R., Mancini, L., Mohammad, S., 2019. Integrating X-ray computed tomography with chemical imaging to quantify mineral re-crystallization from granulite to eclogite metamorphism in the Western Italian Alps (Sesia-Lanzo Zone). Front. Earth Sci. 7, 327. https://doi.org/10.3389/feart.2019.00327.

Dal Piaz, G.V., Bistacchi, A., Gianotti, F., Monopoi, B., Passeri, L., Schivo, A., 2016. Note illustrative del F. 070 Monte Cervino della Carta geologica d'Italia alla scala 1: 50.000, vol. 101. Memorie Descrittive Carta Geologica D`Italia, pp. 5–258.

Daczko, N.R., Piazolo, S., 2022. Recognition of melferite – a rock formed in syn-deformational high-strain melt-transfer zones through sub-solidus rocks: a review and synthesis of microstructural criteria. Lithos 430–431, 106850. https://doi.org/10.1016/j.lithos.2022.106850.

Deer, W.A., Howie, R.A., Zussman, J., 1992. An Introduction to the Rock-Forming Minerals. John Wiley and Sons, New York.

Dewey, J.F., Helman, M.L., Turco, E., Hutton, D.H.W., Knott, S.D., 1989. Kinematics of the western mediterranean. In: Coward, M.P., Dietrich, D., Park, R.G. (Eds.), Alpine Tectonics, vol. 45. Geological Society of London Special Publication, pp. 265–283. https://doi.org/10.1144/GSL.SP.1989.045.01.15.

Diehl, E.A., Masson, R., Stutz, A.H., 1952. Contributo alla conoscenza del ricoprimento della Dent Blanche. Mem.gli Ist. Geol. Mineral. Univ. Padova 17, 1–52.

Etheridge, M.A., Daczko, N.R., Chapman, T., Stuart, C.A., 2021. Mechanisms of melt extraction during lower crustal partial melting. J. Metamorph. Geol. 39 (1), 57–75. https://doi.org/10.1111/jmg.12561.

Fazio, E., Alsop, G.I., Nania, L., Graziani, R., Iaccarino, S., Montomoli, C., Carosi, R., Luzin, V., Salvemini, F., Gambino, S., Cirrincione, R., Mamtani, M.A., 2024. CPO and quantitative textural analyses within sheath folds. J. Struct. Geol. 178, 105000 https://doi.org/10.1016/j.jsg.2023.105000ù.

Forti, L., Brandolini, F., Oselini, V., Peyronel, L., Pezzotta, A., Vacca, A., Zerboni, A., 2023. Geomorphological assessment of the preservation of archaeological tell sites. Sci. Rep. 13, 7683.

Gardien, V., Reusser, E., Marquer, D., 1994. Pre-alpine metamorphic evolution of the gneisses from the valpelline series (western Alps, Italy). Schweizerische Mineralogische und Petrographische Mitteilungen 74, 489–502.

Gosso, G., Rebay, G., Roda, M., Spalla, M.I., Tarallo, M., Zanoni, D., Zucali, M., 2015. Taking advantage of petrostructural heterogeneities in subduction collisional orogens, and effect on the scale of analysis. Per. Mineral. 84 (3), 779–825. https://doi.org/10.2451/2015PM0452.

Grasemann, B., Stüwe, K., Vannay, J.-C., 2003. Sense and non-sense of shear in flanking structures. J. Struct. Geol. 25, 19–34. https://doi.org/10.1016/S0191-8141(02)00012-3.

Handy, M.R., Schmid, S.M., Bousquet, R., Kissling, E., Bernoulli, D., 2010. Reconciling plate-tectonic reconstructions of Alpine Tethys with the geological- geophysical record of spreading and subduction in the Alps. Earth Sci. Rev. 102, 121–158. https://doi.org/10.1016/j.earscirev.2010.06.002.

Heilbronner, R., 2011. Distortion of orientation data introduced by digitizing procedures. J. Microsc. 149 (2), 83–96. https://doi.org/10.1111/j.1365-2818.1988.tb04566.x.

Heilbronner, R., Barrett, S., 2014. Image Analysis in Earth Sciences. Springer, Berlin, Heidelberg. https://doi.org/10.1007/978-3-642-10343-8.

Henry, B., Guidotti, C.V., Thomson, J.A., 2005. The Ti-saturation surface for low-to-medium pressure metapelitic biotite: implications for geothermometry and Ti-substitution mechanisms. Am. Mineral. 90, 316–328. https://doi.org/10.2138/am.2005.1498.

Hopgood, A.M., 1979. Polyphase fold analysis as a means of interpreting the deformational history of migmatites. Geology 31, 109–110.

Hudleston, P.J., 1989. The association of folds and veins in shear zones. J. Struct. Geol. 11 (8), 949–957. https://doi.org/10.1016/0191-8141(89)90046-1.

Johnson, S.E., Vernon, R.H., 1995. Inferring the timing of porphyroblast growth in the absence of continuity between inclusion trails and matrix foliations: can it be reliably done? J. Struct. Geol. 17 (8), 1203–1206. https://doi.org/10.1016/0191-8141(95)00021-5.

Kriegsman, L.M., 2001. Partial melting, partial melt extraction and partial back reaction in anatectic migmatites. Lithos 56 (1), 75–96. https://doi.org/10.1016/S0024-4937(00)00060-8.

Kriegsman, L.M., Alvarez-Valero, A.M., 2010. Meltproducing versus melt-consuming reactions in pelitic xenoliths and migmatites. Lithos 116, 310–320. https://doi.org/10.1016/j.lithos.2009.09.001.

Kunz, B.E., Manzotti, P., von Niederhäusern, B., Engi, M., Darling, J.R., Giuntoli, F., Lanari, P., 2018. Permian high-temperature metamorphism in the western Alps (NW Italy). Int. J. Earth Sci. 107, 203–229. https://doi.org/10.1007/s00531-017-1485-6.

Lanari, P., Vho, A., Bovay, T., Airaghi, L., Centrella, S., 2019. Quantitative compositional mapping of mineral phases by electron probe micro-analyser. Geol. Soc. London Spec. Publ. 478, 39–63.

Lanari, P., Vidal, O., De Andrade, V., Dubacq, B., Lewin, E., Grosch, E.G., Schwartz, S., 2014. XMapTools: a MATLAB©-based program for electron microprobe X-ray image processing and geothermobarometry. Comput. Geosci. 62, 227–240. https://doi.org/10.1016/j.cageo.2013.08.010.

Lardeaux, J.M., 2014. Deciphering orogeny: a metamorphic perspective. Examples from European Alpine and Variscan belts: Part I: alpine metamorphism in the western Alps. A review. Bull. Soc. Geol. Fr. 185 (2), 93–114. https://doi.org/10.2113/gssgfbull.185.2.93.

Le Breton, N.L., Thompson, A.B., 1988. Fluid-absent (dehydration) melting of biotite in metapelites in the early stages of crustal anatexis. Contrib. Mineral. Petrol. 99, 226–237. https://doi.org/10.1007/BF00371463.

Lee, S., Suh, J., Park, H-d., 2013. Smart Compass-Clinometer: a smartphone application for easy and rapid geological site investigation. Comput. Geosci. 61, 32–42. https://doi.org/10.1016/j.cageo.2013.07.014.

Lee, A.L., Lloyd, G.E., Torvela, T., Walker, A.M., 2020. Evolution of a shear zone before, during and after melting. J. Geol. Soc. 177 (4), 738–751. https://doi.org/10.1144/jgs2019-114.

Manzotti, P., Zucali, M., 2013. The pre-Alpine tectonic history of the Austroalpine continental basement in the Valpelline unit (Western Italian Alps). Geol. Mag. 150, 153–172. https://doi.org/10.1017/S0016756812000441.

Manzotti, P., Ballèvre, M., 2017. Tectonic history of the dent blanche. Geol. Field Trips and Maps 9 (2.1), 73. https://doi.org/10.3301/GFT.2017.02.

Manzotti, P., Ballèvre, M., Zucali, M., Robyr, M., Engi, M., 2014a. The tectonometamorphic evolution of the Sesia–Dent Blanche nappes (internal Western Alps): review and synthesis. Swiss J. Geosci. 107 (2), 309–336. https://doi.org/10.1007/s00015-014-0172-x.

Manzotti, P., Zucali, M., Ballèvre, M., Robyr, M., Engi, M., 2014b. Geometry and kinematics of the roisan-cignana shear zone, and the orogenic evolution of the dent blanche tectonic system (western Alps). Swiss J. Geosci. 107, 23–47. https://doi.org/10.1007/s00015-014-0157-9.

Manzotti, P., Ballèvre, M., Pitra, P., Benita Putlitz, P., Robyr, M., Müntener, O., 2020. The growth of sodic amphibole at the greenschist- to blueschist-facies transition (dent blanche, western Alps): bulk-rock chemical control and thermodynamic modelling. J. Petrol. 61 (4) https://doi.org/10.1093/petrology/egaa044.

Mattéo, L., Manighetti, I., Tarabalka, Y., Gaucel, J.-M., van den Ende, M., Mercier, A., Tasar, O., Girard, N., Leclerc, F., Giampetro, T., Dominguez, S., Malavielle, J., 2021. Automatic fault mapping in remote optical images and topographic data with deep learning. J. Geophys. Res. Solid Earth 126, e2020JB021269. https://doi.org/10.1029/2020JB021269.

Midland Valley, 2015. FieldMove User Guide.

Misra, A.A., Mukherjee, S., 2023. Atlas of Structural Geological and Geomorphological Interpretation of Remote Sensing Images. Wiley and Sons. https://onlinelibrary.wiley.com/doi/book/10.1002/9781119813392.7.

Mukherjee, S., 2014. Review of the flanking structures in meso- and micro-scales. Geol. Mag. 151, 957–974. https://doi.org/10.1017/S0016756813001088.

Nicot, E., 1977. Les roches meso et catazonales de la Valpelline (nappe de la Dent Blanche, Alpes italiennes) (PhD Thesis, Paris).

Niedzielski, T., 2018. Applications of unmanned aerial vehicles in geosciences: introduction. Pure Appl. Geophys. 175, 3141–3144. https://doi.org/10.1007/s00024-018-1992-9.

Novakova, L., Pavlis, T.L., 2017. Assessment of the precision of smart phones and tablets for measurement of planar orientations: a case study. J. Struct. Geol. 97, 93–103. https://doi.org/10.1016/j.jsg.2017.02.015.

Ogiermann, J., Kalt, A., 2000. Chemical characterization of cordierite breakdown products in gneisses and migmatites of the schwarzwald and the bayerische wald. J. Conf. Abstr. 5 (2), 752.

Ortolano, G., Visalli, R., Gaston, G., Cirrincione, R., 2018. Quantitative X-ray map analyser (Q-XRMA): a new GIS-based statistical approach to mineral image analysis. Comput. Geosci. 115, 56–65. https://doi.org/10.1016/j.cageo.2018.03.001.

Palin, R.M., Weller, O.M., Waters, D.J., Dyck, B., 2016. Quantifying geological uncertainty in metamorphic phase equilibria modelling; a Monte Carlo assessment and implications for tectonic interpretations. Geosci. Front. 7 (4), 591–607. https://doi.org/10.1016/j.gsf.2015.08.005.

Passchier, C.W., Trouw, R.A.J., 2005. Microtectonics. Springer, Berlin, Heidelberg. https://doi.org/10.1007/3-540-29359-0.

Pennacchioni, G., Guermani, A., 1993. The mylonites of the austroalpine dent blanche nappe along the northwestern side of the valpelline valley (Italian western Alps). Mem. Sci. Geol. 45, 37–55.

Perego, A., Zerboni, A., Cremaschi, M., 2011. Geomorphological map of the messak settafet and mellet (central sahara, SW Libya). J. Maps 7 (1), 464–475. https://doi.org/10.4113/jom.2011.1207.

Pesenti, C., Zucali, M., Manzotti, P., Diella, V., Risplendente, A., 2012. Linking U-Th-Pb monazite dating to partial melting microstructures: application to the Valpelline series (Austroalpine domain, Western Alps). Rend. Online Soc. Geol. It. 22, 183–185.

QGIS Development Team. 2024. Available onlone: https://qgis.org/en/site/. (accessed 21.03.24.).

Ramsay, J.G., Huber, M.I., 1987. The Techniques of Modern Structural Geology: Folds and Fractures. Academic Press.

Roda, M., Spalla, M.I., Filippi, M., Lardeaux, J.-M., Rebay, G., Regorda, A., Zanoni, D., Zucali, M., Gosso, G., 2023. Metamorphic remnants of the Variscan orogeny across the Alps and their tectonic significance. Geosciences 13, 300. https://doi.org/10.3390/geosciences13100300.

Roda, M., Zucali, M., 2008. Meso and microstructural evolution of the Mont morion metaintrusives complex (dent blanche nappe, austroalpine domain, valpelline, western Italian Alps). Ital. J. Geosci. 127, 105–123.

Roda, M., Zucali, M., 2011. Tectono-metamorphic map of the Mont morion permian metaintrusives (Mont morion - Mont collon - matterhorn complex, dent blanche unit), valpelline - western Italian Alps. J. Maps 7, 519–535. https://doi.org/10.4113/jom.2011.1194.

Roda, M., Zucali, M., Corti, L., Visalli, R., Ortolano, G., Spalla, M.I., 2021. Blueschist mylonitic zones accommodating syn-subduction exhumation of deeply buried continental crust: the example of the Rocca Canavese Thrust Sheets Unit (Sesia-Lanzo Zone, Italian Western Alps). Swiss J. Geosci. 114, 6–39. https://doi.org/10.1186/s00015-021-00385-7.

Salvi, F., Spalla, M.I., Zucali, M., Gosso, G., 2010. Three-dimensional evaluation of fabric evolution and metamorphic reaction progress in polycyclic and polymetamorphic terrains: a case from the Central Italian Alps. In: Spalla, M.I., Marotta, A.M., Gosso, G. (Eds.), Advances in Interpretation of Geological Processes, vol. 334, pp. 173–187. https://doi.org/10.1144/SP332.11.

Sawyer, E.W., 2001. Melt segregation in the continental crust: distribution and movement of melt in anatectic rocks. J. Metamorph. Geol. 19, 291–309. https://doi.org/10.1046/j.0263-4929.2000.00312.x.

Sawyer, E.W., 2008. Working with migmatites. In: Short Course Series: Mineralogical Association of Canada, vol. 38. Mineralogical Association of Canada, Quebec.

Schmid, S.M., Fügenschuh, B., Kissling, E., Schuster, R., 2004. Tectonic map and overall architecture of the Alpine orogen. Eclogae Geol. Helv. 97, 93–117. https://doi.org/10.1007/s00015-004-1113-x.

Seifert, F., Schreyer, W., 1970. Lower temperature stability limit of Mg cordierite in the range 1-7 kbar water pressure: a redetermination. Contrib. Mineral. Petrol. 27, 225–238. https://doi.org/10.1007/BF00385779.

Spalla, M.I., 1993. Microstructural control on the P-T path construction in metapelites from the austroalpine crust (texel gruppe, eastern Alps). Schweizerische Mineralogische und Petrographische Mitteilungen 73 (2), 259–275. https://doi.org/10.5169/seals-55573.

Spalla, M.I., Zucali, M., Di Paola, S., Gosso, G., 2005. A critical assessment of the tectono-thermal memory of rocks and definition of tectono-metamorphic units: evidence from fabric and degree of metamorphic transformations. Geol. Soc. Spec. Publ. 243 (1), 227–247. https://doi.org/10.1144/GSL.SP.2005.243.01.16.

Spear, F., 1994. Metamorphic phase equilibria and pressure-temperature-time paths. Mineral. Soc. Monographs 799.

Tavani, S., Granado, P., Corradetti, A., Girundo, M., Iannace, A., Arbués, P., Muñoz, J.A., Mazzoli, S., 2014. Building a virtual outcrop, extracting geological information from it, and sharing the results in Google Earth via OpenPlot and Photoscan: an example from the Khaviz Anticline (Iran). Comput. Geosci. 63, 44–53. https://doi.org/10.1016/j.cageo.2013.10.013.

Tavani, S., Corradetti, A., Billi, A., 2016. High precision analysis of an embryonic extensional fault-related fold using 3D orthorectified virtual outcrops: the viewpoint importance in structural geology. J. Struct. Geol. 86, 200–210. https://doi.org/10.1016/j.jsg.2016.03.009.

Tavani, S., Billi, A., Corradetti, A., Mercuri, M., Bosman, A., Cuffaro, M., Seers, T., Carminati, E., 2022. Smartphone assisted fieldwork: towards the digital transition of geoscience fieldwork using LiDAR-equipped iPhones. Earth Sci. Rev. 227, 103969 https://doi.org/10.1016/j.earscirev.2022.103969.

Thiele, S.T., Grose, L., Samsu, A., Micklethwaite, S., Vollgger, S.A., Cruden, A.R., 2017. Rapid, semi-automatic fracture and contact mapping for point clouds, images and geophysical data. Solid Earth 8, 1241–1253. https://doi.org/10.5194/se-8-1241-2017.

Visalli, R., Ortolano, G., Godard, G., Cirrincione, R., 2021. Micro-fabric analyzer (MFA): a new semiautomated ArcGIS-based edge detector for quantitative microstructural analysis of rock thin-sections. ISPRS Int. J. Geo-Inf. 10, 51. https://doi.org/10.3390/ijgi10020051.

Waters, D.J., 2001. The significance of prograde and retrograde quartz-bearing intergrowth microstructures in partially melted granulite-facies rocks. Lithos 56, 97–110. https://doi.org/10.1016/S0024-4937(00)00061-X.

Westoby, M.J., Brasington, J., Glasser, N.F., Hambrey, M.J., Reynolds, J.M., 2012. 'Structure-from-Motion'photogrammetry: a low-cost, effective tool for geoscience applications. Geomorphology 179, 300–314. https://doi.org/10.1016/j.geomorph.2012.08.021.

White, R.W., Powell, R., Holland, T.J.B., Johnson, T.E., Green, E.C.R., 2014. New mineral activity–composition relations for thermodynamic calculations in metapelitic systems. J. Metamorph. Geol. 32, 261–286. https://doi.org/10.1111/jmg.12071.

Whitney, D.L., Evans, B.W., 2010. Abbreviation for names of rock-forming minerals. Am. Mineral. 95, 185–187. https://doi.org/10.2138/am.2010.3371.

Yakymchuk, C., 2020. Migmatites. In: Alderton, D., Elias, S.A. (Eds.), Enciclopedia of Geology, second ed. Academic press, pp. 492–501. https://doi.org/10.1016/B978-0-08-102908-4.00021-7.

Zerboni, A., Perego, A., Cremaschi, M., 2015. Geomorphological map of the tadrart acacus massif and the Erg Uan kasa (Libyan central sahara). J. Maps 11 (5), 772–778. https://doi.org/10.1080/17445647.2014.955891.

Zucali, M., Spalla, M.I., Gosso, G., 2002. Strain partitioning and fabric evolution as A correlation tool: the example of the eclogitic micaschists complex in the SesiaLanzo Zone (Monte Mucrone e Monte Mars, Western Alps Italy). Schweizerische Mineralogische und Petrographische Mitteilungen 82, 429–454.

Zucali, M., Manzotti, P., Diella, V., Pesenti, C., Risplendente, A., Darling, J., Engi, M., 2011. Permian tectonometamorphic evolution of the dent-blanche unit (austroalpine domain, western Italian Alps). Rend. Online Soc. Geol. It. 15, 133–136.

Zucali, M., Corti, L., Delleani, F., Zanoni, D., Spalla, M.I., 2020. 3D reconstruction of fabric and metamorphic domains in a slice of continental crust involved in the Alpine subduction system: the example of Mt. Mucrone (Sesia–Lanzo Zone, Western Alps). Int. J. Earth Sci. 109 (4), 1337–1354. https://doi.org/10.1007/s00531-019-01807-6.

Zucali, M., Corti, L., Roda, M., Ortolano, G., Visalli, R., Zanoni, D., 2021. Quantitative X-ray maps analysis of composition and microstructure of permian high-temperature relicts in acidic rocks from the sesia-lanzo zone eclogitic continental crust, western Alps. Minerals 11, 1421. https://doi.org/10.3390/min11121421.

Zucali, M., 2023. pyMinColab. Available at: https://github.com/mzucali/pyMinColab/. (accessed 14.07.23.).

3D scanner App©. 2024. Available online: https://3dscannerapp.com/. (accessed 21.03.24.).